In vivo physiology of foveal retinal ganglion cells in *Macaca fascicularis*

Authors note: This is a working draft of the manuscript, on which we welcome comments and questions. We will be updating this preprint periodically as we work towards a full and complete manuscript, and in particular, updating the modeling results and the Discussion section as we refine and finalize the model.

Tyler Godat*[1,2], Nicolas P. Cottaris[3], Sara Patterson[1], Kendall Kohout[1,2], Keith Parkins[1], Qiang Yang[1], Jennifer M. Strazzeri[1,4], Juliette E. McGregor[1], David H. Brainard[3], William H. Merigan*[1,4] & David R. Williams[1,2,4]

[1] Center for Visual Science, University of Rochester, Rochester, NY, United States of America.

[2] Institute of Optics, University of Rochester, Rochester, NY, United States of America.

[3] Department of Psychology, University of Pennsylvania, Philadelphia, PA, United States of America.

[4] David & Ilene Flaum Eye Institute, University of Rochester Medical Center, Rochester, NY, United States of America.

* Corresponding author

E-mail: tgodat@ur.rochester.edu (TG), wmerigan@ur.rochester.edu (WHM)

Funding: This work was supported by The National Eye Institute https://nei.nih.gov/about through grants NIH EY007125 to TG, NIH U01EY025497 to DRW, NIH EY031467 to DRW, NIH

EY021166 to WHM, and through an unrestricted grant to the Flaum Eye Institute from Research to Prevent Blindness https://www.rpbusa.org/rpb/grants-and-research/grants/institutional-grants/. This work was also supported by funding from Facebook Reality Labs to DHB. The funders had no role in study design, data collection and analysis, decision to publish, or preparation of the manuscript.

Competing Interest Statement: I have read the journal's policy and the authors of this manuscript have the following competing interests: D.R.W. and W.H.M. receive funding from the National Eye Institute. D.R.W. receives additional funding from The Arnold and Mabel Beckman Foundation, Alcon, and Warby Parker, and W.H.M. receives funding from Research to Prevent Blindness. D.H.B. receives funding from the National Institutes of Health, Johnson & Johnson, and Facebook Reality Labs. D.R.W. has patents with the University of Rochester for adaptive optics imaging of the retina: US patent #6,199,986 "Rapid, automatic measurement of the eye's wave aberration". US patent #6,264,328 "Wavefront sensor with off-axis illumination" and US patent 6,338,559 "Apparatus and method for improving vision and retinal imaging". Q.Y. has patents with the University of Rochester, Canon Inc. and the University of Montana, for image stabilization algorithms: US patent #9,226,656: "Real-time optical and digital image stabilization for adaptive optics scanning ophthalmoscopy", US patent # 9,406,133: "System and method for real-time image registration", US patent #: 9,485,383, "Imaging based correction of distortion from a scanner" and US patent #:9,454,084, "Light source modulation for a scanning microscope". D.H.B. is an inventor on US patent App. 16/389,942. Additionally Q.Y. has undertaken consultancy work for Oculus VR and Boston Micromachine Corporation. This does not alter our adherence to PLOS ONE policies on sharing data and materials.

Abstract

The primate fovea is specialized for high-resolution spatial and chromatic vision, possessing a unique topography characterized by a pit in which the inner retina and associated vasculature have been excavated, the highest density of cones anywhere in the retina, and a disproportionately large representation in visual cortex. The crucial visual properties conferred by the fovea are mediated by retinal ganglion cells (RGCs) the somas of which lie at the margin of the foveal pit. Microelectrode recordings of these centermost retinal ganglion cells have been challenging due to the fragility of the fovea in the excised retina. This has been overcome in this study by combining high resolution fluorescence adaptive optics ophthalmoscopy with calcium imaging to optically record functional responses of foveal RGCs to visual stimuli in the living eye. Here we use this approach to study the chromatic responses of RGCs to uniform fields modulated in different directions in color space and achromatic responses with monochromatic drifting gratings. We repeated these recordings in many cells in each of three *macaca fasicularis* primates over weeks or months. We find that most of the L/M chromatically opponent cells serving the most central cones respond to high spatial frequencies, reflecting strong surround inhibition that sacrifices sensitivity at low frequencies in favor of the transmission of fine detail in the retinal image. In addition, we find the L/M cells vary in spatial frequency bandwidths, suggesting that L/M chromatic opponency, often considered largely due to input from single cones, has more diverse receptive field structure than previously thought. By characterizing the functional properties of retinal ganglion cells *in vivo* through adaptive optics, we provide a lower bound on the response characteristics of these cells *in situ* and their role in vision processing.

Introduction

66 In primates, the fovea is a specialized region of the retina characterized by a high density of cones
67 at its center and a corresponding outward displacement of inner retinal cells and retinal
68 vasculature. These specializations, along with a vastly expanded representation in cortex [1-3],
69 contribute to the superiority of foveal vision relative to peripheral vision in spatial resolution and
70 color discrimination [1, 4-20]. The 20 or more classes of retinal ganglion cells (RGCs) that have
71 been identified in macaque retina [1, 4, 6, 7, 13, 17-51] reflect a complex array of retinal
72 computations that precede additional processing in the brain, but a complete understanding of
73 these independent circuits and their role in vision and behavior has proven elusive. Even the
74 precise role and scope of function of the most numerous and commonly studied RGCs, the midget
75 ganglion cells, remains controversial. Some have argued that the midget pathway is solely
76 specialized for so called "red-green" color vision [4, 24, 52], others have argued that midgets are
77 responsible for mediating only achromatic spatial acuity [53, 54], and still others have argued that
78 midget RGCs do "double-duty" by transmitting both chromatic and achromatic information
79 postreceptorally [55-57]. One additional hypothesis holds that there are two subclasses of midget
80 cells—one responsible for chromatic vision and the other for achromatic vision [47, 58].
81
82 Physiological responses from and morphologies of primate RGCs have been studied *in vivo* with a
83 microelectrode that penetrates the sclera [59, 60] as well as *in vitro* using a single microelectrode
84 [6, 26] or microelectrode arrays [61, 62]. However, the majority of recordings in primate have
85 been made in peripheral retina, often 30 to 70 degrees from the fovea because of the difficulty
86 penetrating the internal limiting membrane near the fovea. Moreover, the survival of an excised
87 fovea is temporally constrained and the curved structure of the foveal pit is often strained when
88 flattened, sometimes tearing crucial circuitry. While the anatomical basis for foveal circuitry has
89 been studied extensively [7, 31, 33, 37, 56, 63] and there has been some *ex vivo* physiology of

90 foveal RGCs, most individual cell classes present in the primate fovea have not been directly
91 studied at the most central locations. Retinal processing can be studied by recording in the LGN,
92 but the foveal representation of the LGN is located within a relatively thin cell layer making such
93 recordings challenging [64]. Moreover, it has been difficult to identify the exact foveal center and
94 therefore the precise retinal eccentricity of single cell recordings in LGN [5, 9, 65-67].
95
96 In this study, we use functional adaptive optics cellular imaging in the living eye (FACILE) [12, 16,
97 68, 69], a technique that utilizes an adaptive optics light scanning ophthalmoscope (AOSLO) to
98 image fluorescence elicited from the activity of RGCs that express genetically encoded calcium
99 indicators such as those described in Chen et al [70]. The lateral resolution of the instrument
100 (0.5µm-1.5µm depending on the field of view or imaging paradigm) is such that we can image
101 even the smallest foveal cones and precisely locate the fovea using cone density [16] and by
102 locating the center of the avascular zone. Using this technique, we can both image and stimulate
103 the centermost foveal cones with spatial and chromatic stimuli and optically record the activity
104 of the ganglion cells that serve them, revealing *in vivo* functional physiology of the innermost
105 foveal primate RGCs. Indeed, we can return repeatedly to the same ganglion cells for weeks to
106 months, allowing repeated measures of the same cells and making possible the tracking of
107 functional changes over time.
108
109 **Materials and Methods**
110
111 **Animal Care**. The macaques (*Macaca fascicularis)* were housed in pairs in an AAALAC accredited
112 institution. They had free access to food and water providing a complete, nutritious diet.
113 Supplementing their ordinary lab chow, animals were given various treats daily, such as: nuts,

114 raisins, and a large variety of fresh fruits and vegetables. An animal behaviorist provided novel
115 enrichment items once per week, including items like grass and treat filled bags, grapevines, and
116 forage boxes. Daily enrichment included several pieces of manipulata: mirrors, puzzle feeders
117 rotated among the animals, daily movies and/or music, as well as rotating access to a large free-
118 ranging space with swings and elevated perches during long periods between imaging sessions.
119 All macaques were cared for by the Department of Comparative Medicine veterinary staff,
120 including four full-time veterinarians, five veterinary technicians, and an animal care staff who
121 monitored animal health and checked for signs of discomfort at least twice daily. This study was
122 carried out in strict accordance with the Association for Research in Vision and Ophthalmoscopy
123 (ARVO) Statement for the Use of Animals and the recommendations in the Guide for the Care and
124 Use of Laboratory Animals of the National Institutes of Health. The protocol was approved by the
125 University Committee on Animal Resources of the University of Rochester (PHS assurance
126 number: D16-00188(A3292-01)).
127
128 **Immune Suppression**. Three different macaques (M1, M2, M3) received varying amounts of
129 Cyclosporine A prior to intravitreal injection and onset of imaging. All doses were delivered
130 subcutaneously, and blood trough levels were collected weekly to titrate the dose into a
131 therapeutic range of 150-200 ng ml^{-1} and then maintained at that level. M1 did not receive any
132 immune suppression. M2 began immune suppression in March 2018 with 6 mg kg^{-1}, then stepped
133 down a month later to 4 mg kg^{-1} which was maintained until October 2019 when suppression was
134 stopped; we believe that the cessation of immune suppression was responsible for widespread
135 apparent death of foveal ganglion cells some months later in this animal (data not shown in this
136 manuscript). M3 started immune suppression in May 2019 at 6 mg kg^{-1}, then stepped down to 3.4
137 mg kg^{-1} which continues at time of submission.

138

139 **AAV mediated gene delivery to retina**. Intravitreal injections were carried out in each animal as
140 previously described [71]. In M1, *7m8-RGC-GCaMP6f* was injected into the right eye; *AAV2-CAG-*
141 *GCaMP6s* was injected into the left eye of M2 and into the right eye of M3. All vectors were
142 synthesized by the University of Pennsylvania Vector Core. Before the injections, the eyes were
143 sterilized with 50% diluted Betadine, and the vector was injected into the middle of the vitreous
144 at a location approximately 4mm behind the limbus using a tuberculin syringe and 30 gauge
145 needle. Following injection, each eye was imaged weekly for several months with a conventional
146 scanning light ophthalmoscope (Heidelberg Spectralis) using the 488nm autofluorescence
147 modality to determine onset of GCaMP expression, image quality, and monitor eye health.

148

149 **Anesthesia and animal preparation.** All monkeys were fasted from 4-18 hours prior to anesthesia
150 induction. For HRA and Fundus imaging using the Heidelberg instrument, induction began with 6
151 mg kg^{-1} Ketamine plus 0.15 mg kg^{-1} Medetomidine and was reversed with 0.2 mg kg^{-1} Antisedan.
152 During AOSLO imaging, anesthesia induction began with 10 mg kg^{-1} Ketamine, 0.25 mg kg^{-1}
153 Midazolam, and 0.017 mg kg^{-1} Glycopyrrolate intramuscularly. The animal was then given 5 mg
154 kg^{-1} Ketofen intramuscularly to prevent pain or inflammation from a lid speculum being placed in
155 the eye during imaging for an extended period.

156

157 The pupil was dilated with a combination of Tropicamide 1% and Phenylephrine 2.5%. In cases of
158 minimal pupil dilation within the standard amount of time, Phenylephrine 10% and/or
159 Cyclopentolate 1% drops were also administered to complete dilation. Both eyes were covered
160 with a hydrating ophthalmic gel (Systane Gel). The target eye then had the lid speculum placed to
161 keep the eye open during imaging, and a sterile contact lens was placed to ensure corneal

162 protection and minimize optical aberrations. The fellow eye was taped closed with porous tape
163 to protect the cornea from drying.
164
165 The animal was placed prone onto a custom stereotaxic cart. Prior to intubation, an oxygen mask
166 with 1-2% Isoflurane was placed over the animal's face to allow for adequate sedation. An
167 intravenous drip of Lactated Ringers with 5% Dextrose was maintained at 5 ml kg^{-1} h^{-1} for the
168 duration of imaging. The animal was intubated and maintained at a surgical plane of anesthesia
169 with Isoflurane 1.0-2.5%. A Bair Hugger warming system was placed over the animal to maintain
170 body temperature. Monitoring devices including: rectal temperature probe, blood pressure cuff,
171 electrocardiogram leads, capnograph, and a pulse oximeter, were used to ensure proper
172 monitoring of all vitals. Temperature, heart rate and rhythm, respirations and end tidal CO_2, blood
173 pressure, SPO_2, and reflexes were monitored consistently and recorded every fifteen minutes.
174
175 After a surgical plane of anesthesia was established, the animal was given a 300 mcg kg^{-1} bolus of
176 Rocuronium that was mixed to a concentration of 800 mcg ml^{-1}, followed by an intravenous
177 infusion of 300 mcg kg^{-1} h^{-1}. Once respirations ceased, the animal was maintained on a ventilator
178 until imaging was complete and the infusion was turned off. Once a peripheral nerve response
179 was established an intravenous dose of Glycopyrrolate 0.01 mg kg^{-1} was given. Five minutes after
180 the Glycopyrrolate, Neostigmine 0.05 mg kg^{-1} was given intravenously. The animal was monitored
181 for indications of breathing against the ventilator and then removed from the ventilator once able
182 to breathe without assistance. The animal was removed from the Isoflurane no sooner than
183 fifteen minutes after the Neostigmine injection to ensure stability off the ventilator. The animal
184 was then allowed to wake up and extubated once all reflexes had returned.
185

186 **Adaptive optics imaging.** Data was collected using an AOSLO system previously described in Gray
187 et al. [68]. An 847 nm diode laser source (QPhotonics) was used as a beacon for a Shack-Hartmann
188 Wavefront Sensor (SHWS) to measure optical aberrations in each animal's eye in real time and a
189 Deformable Mirror (ALPAO) was used to correct those aberrations in a closed loop. A 796 nm
190 superluminescent diode source (Superlum) was focused on the photoreceptor layer of the retina
191 to collect reflectance images at an approximately 2 airy disk confocal pinhole, with the images
192 used for both placement of stimuli and later registration of fluorescence images. A 561 nm laser
193 (Toptica) and three LEDs (Thorlabs, center wavelengths 420 nm, 530 nm, 660 nm) were used for
194 visual stimulation of foveal cones. A 488 nm laser source (Qioptiq) was focused on the ganglion
195 cell layer to excite GCaMP fluorescence, which was detected through a 520/35 nm emission filter
196 at an approximately 2 airy disk confocal pinhole for animals M2 and M3 and an approximately 7.5
197 airy disk confocal pinhole for animal M1, each of which was chosen to balance the tradeoff
198 between signal strength and axial resolution. The 488 nm excitation light was presented only
199 during forward scans and filled only the portion of the imaging window where ganglion cells were
200 present to avoid exposing foveal photoreceptors and biasing stimulation. The imaging light
201 intensities at the cornea were 3.4 mW cm^{-2} in M1, 3.2 mW cm^{-2} in M2, and 1.7 mW cm^{-2} in M3 at
202 a dilated pupil size of approximately 6.7mm for each animal. Retinal subtenses were 780 x 570
203 µm in M1, 765 x 560 µm in M2, and 740 x 540 µm or 505 x 380 µm in M3.
204
205 **Light safety.** The total retinal exposure to all light sources (nominally 488 nm at 25 µW, 561 nm
206 at 5 µW, 796 nm at 250 µW, 847 nm at 30 µW, and combined 5 µW from the LEDs at 420 nm, 530
207 nm, and 660 nm) was calculated for each proposed retinal location before each imaging session
208 after measuring the optical power of each source at the pupil plane. Imaging sessions were at
209 least five days apart, so accumulated exposure was not taken account into the calculations. For

210 all animals, the total exposure was kept below the maximum permissible exposure for human
211 retina according to the American National Standards Institute [72-74] further scaled by the
212 squared ratio of the numerical aperture of the human eye to the primate eye (~0.78) [75].
213
214 **Methods to maximize optical quality and signal across experiments.** Our method affords the
215 advantage of being able to record from hundreds of cells simultaneously, but there is a tradeoff.
216 It is known that the retinal ganglion cell layer can be several cells thick especially near the fovea
217 [25, 45]. The best axial resolution that can be achieved with the confocal AOSLO required for our
218 experiments is 25-30 microns, approximately the diameter of 2-3 RGC somas [26], which means
219 that in areas where the RGC layer is thick there will be some optical crosstalk of multiple cells
220 contributing to recorded responses. Therefore, as part of the validation of our method and to be
221 certain in describing the physiology of individual cells, we operate in two distinct modalities. The
222 first modality is a wide field of view (FOV) of 3.70 x 2.70 deg where we can image hundreds of
223 RGCs across the entire width of soma locations (in M1, M2 and M3), but not be certain that each
224 cell is free of crosstalk. The second modality is a smaller FOV of 2.54 x 1.92 deg that is focused
225 only on the innermost foveal slope (only in M3), where the RGCs are in a monolayer—here we
226 can only image tens of cells at a time, but we are certain that they are not contaminated by optical
227 crosstalk. To that end, wide field data is shown from all three animals to show cell populations
228 and general physiology, while data from the smaller field is shown only in animal M3 to draw
229 conclusions about the physiology of individual cells, and in fact, the very innermost foveal RGCs
230 driven by the centermost cones.
231
232 In addition to optical crosstalk, there are several other challenges common to ophthalmic imaging
233 techniques that we needed to overcome for our method. Wavefront correction is at 847 nm,

imaging of the photoreceptor mosaic is accomplished at 796 nm, but stimulation of the photoreceptors using the gratings is at 561 nm and imaging of the ganglion cells is at 488 nm, meaning that there is chromatic aberration between the four channels. In this paradigm, all stimuli were large enough to cover the foveal avascular zone, so transverse chromatic aberration is not an issue as it might be in the case of stimulating single cones, but longitudinal chromatic aberration was accounted for by adjusting source and detector positions along the optical axis using the chromatic dispersion data in humans [76] scaled for the macaque eye. These calculated positions were used as a starting point and further optimized in a model eye prior to imaging and again *in vivo* using algorithms such as simplex [77] to optimize source and detector positions for the best signal. For the data in M3 at the inner edge of the foveal slope, a separate experiment used the responses of 37 cells to 28 c/deg drifting gratings at 6 Hz to empirically find the best axial source position for the 488 nm imaging laser since cells on or near the foveal slope might have differing axial positions in the retina.

As a side effect of the *in vivo* viewing eye being held open for long periods of time during imaging sessions, optical quality tends to degrade over the course of the experiment, slowly at first, but more quickly after the first hour of imaging. To mitigate this, all grating stimuli were presented at the beginning of a session when optical quality was the highest, and only for the first 30 minutes, so that we could ensure the degradation did not preferentially affect high spatial frequency responses.

Lastly, the isoplanatic patch size of our system is approximately 1-1.5 deg, which is smaller than both of the imaging fields (3.70 x 2.70 deg and 2.54 x 1.92 deg) used in this study, producing field aberrations towards the edges of the images, where some ganglion cells were imaged, or cones

258 were stimulated. This, coupled with the fact that the wavefront correction is at a different
259 wavelength than stimulation, means that there could be defocus or higher order residual
260 aberrations that preferentially weaken the presentation of high spatial frequency gratings. Great
261 care was taken to mitigate or optimize all of these mentioned sources of blur, but they cannot all
262 be accounted for in our current instrument, so the spatial frequency responses we measured
263 represent lower bounds of the true cell responses *in vivo* when all sources of blur are removed.
264
265 **Chromatic Stimuli**. To drive the chromatic responses of RGCs connected to foveal photoreceptors,
266 we presented to the fovea a 1.3 deg diameter temporally modulated sinusoidal LED stimulus
267 (Thorlabs, center wavelengths 420nm, 530nm, 660nm) in a Maxwellian view system [78] with
268 mean intensities (measured at the 6.7 mm pupil as above) of 6.8 mW cm^{-2} at 0.2Hz in M1, 7.0 mW
269 cm^{-2} at 0.2Hz in M2, and 7.6 mW cm^{-2} at 0.15Hz in M3. The slow temporal frequencies were chosen
270 to accommodate the slow temporal response of the GCaMP calcium indicators [70] expressed in
271 the RGCs and were adjusted by 0.5 Hz in M3 to avoid potential confound with the respiration rate
272 in that animal. The source wavelengths were chosen to maximize interaction with cone
273 photopigments [79] while minimizing significant confound by macular pigment absorption, the
274 spatial distribution of which was not measured in this study [80, 81]. Wavelengths were also
275 chosen to stay within the transmittance range of the anterior optics [82]. Each presentation was
276 90s long following a 30s adaptation period in which the mean luminance white point and imaging
277 laser were on. The cone fundamentals were constructed using the standard template [83, 84] and
278 the center wavelengths for macaque primates [85]. The transmissivity of the eye (including
279 cornea, aqueous, lens, and vitreous) was modeled using measured data from the rhesus [82]. For
280 the luminous efficiency function, an equal weighting of the M and L cone fundamentals was used
281 as the ratio of L and M cones in macaques is close to unity on average [86]. The LEDs were

282 calibrated using a spectrometer (Ocean Optics) validated by a NIST traceable blackbody source.
283 There were five stimuli presented in this way to the animals, all utilizing silent substitution [87]
284 and the Psychophysics Toolbox [88] to calculate the appropriate power modulations needed: an
285 isoluminant stimulus targeting both L and M cones in counterphase (L modulation 15%, M
286 modulation 17%), an L cone isolating stimulus (24% modulation), an M cone isolating stimulus
287 (33% modulation), an S cone isolating stimulus (92% modulation), and a Luminance stimulus
288 (100% modulation, all cone classes). Within one experiment, each of the stimuli used in that
289 experiment were presented three times and responses were averaged within the experiment. In
290 M1, only one experiment was performed. In M2 and M3, two experiments across the entire width
291 of soma locations were performed and responses across sessions were averaged. In M3, three
292 separate experiments at the innermost foveal RGCs were performed and averaged.
293
294 **Grating Stimuli.** To probe the spatial configuration of foveal RGC receptive fields, we presented
295 1.9 deg in extent monochromatic (561nm) drifting gratings at 6Hz that were sinusoidal with 100%
296 contrast and mean intensities (measured at the pupil of 6.7 mm) of 1.72 mW cm^{-2} in M2, 1.8 mW
297 cm^{-2} in M3, and 3.2 mW cm^{-2} (large field of view condition) and 1.3 deg in extent in M3 in a small
298 field of view condition that imaged only the innermost RGCs closest to the fovea. These visual
299 stimuli at 6 Hz were too fast for GCaMP to track modulation, so cellular responses were
300 characterized by a sustained increase in fluorescence during stimulation as opposed to
301 modulation. Stimuli were 45s in length with a 15s adaptation period to the mean luminance of
302 the stimulus laser and imaging laser. In both animals tested, a control and 14 different gratings
303 were presented that ranged from 2 cycles/deg to 34 cycles/deg; each grating was presented twice
304 within a session and responses were averaged. In the smaller field of view in M3, the increased
305 resolution meant that the spatial frequency range was stretched from 4 cycles/deg to 49

306 cycles/deg. Again, a control and 14 different gratings were presented twice each within a session
307 and responses were averaged. There were three such sessions in M3, and the variability and
308 averages are shown in the results. The presentation of a flat field with 0% modulation functioned
309 as a control for each RGC to determine whether a response to the other spatial frequencies was
310 significant. No data from drifting gratings is shown for animal M1, as the signal was too weak and
311 noisy to produce reliable data from these stimuli. We note that as gratings were only presented
312 in one orientation, the responses of some cells could be lessened if they possessed orientation
313 sensitivity [89].
314
315 **Data analysis**. To remove blurring and other effects of residual eye movements present in the raw
316 recordings, each video frame of the fluorescence recording was co-registered using corresponding
317 frames from a high signal-to-noise reflectance video of the photoreceptor layer at the same
318 retinal location. During imaging, a reference frame was taken in the reflectance channel to allow
319 for real-time stabilization; this reference frame was also used as the reference for the frame-to-
320 frame cross-correlation method image registration [90] of all videos taken at that location. One
321 registered video, typically one of the videos corresponding to the peak spatial frequency response
322 (usually 10 – 30 cycles/deg), was temporally summed to create a high signal-to-noise ratio
323 fluorescence image of the ganglion cell layer, and individual ganglion cells were segmented using
324 the open source software GIMP. Typically, all identifiable cells in the focal plane were segmented,
325 though sometimes cells were excluded if the boundaries between two or more adjacent cells were
326 unclear. The segmentation mask from GIMP was exported to MATLAB, where it was applied to all
327 registered videos at that location to isolate data from individual RGCs. For every frame, the mean
328 of the signal within each cell mask was computed to produce an average signal timecourse for

329 each cell. When the same stimuli were repeated across multiple sessions, the timecourses for
330 each cell were averaged across all sessions.
331
332 To estimate cell soma sizes, two independent segmentation methods were respectively used by
333 two different observers, and soma sizes for cells from the L/M opponent, Luminance only, S only,
334 and L/M/S functional groups (based on the chromatic stimuli) were compared using the data
335 obtained with segmentation method. A Wilcoxon rank-sum test, equivalent to a Mann-Whitney
336 U test (MATLAB function ranksum(x,y)) was used to determine statistical significance for whether
337 or not the functional groupings exhibited different size distributions.
338
339 For the chromatic/achromatic data, the temporal speed of the flicker (0.15-0.20 Hz) was well
340 within the temporal resolution of the GCaMP6, so cells responding to the stimulus exhibited a
341 quasi-sinusoidal modulation in fluorescence level where the amplitude and phase depended on
342 the receptive field of the cell and the frequency depended on the stimulus frequency. Each cell
343 timecourse was filtered using a Hann windowing function before being Fourier transformed into
344 the frequency domain. The Fourier amplitudes were normalized by subtracting out the mean
345 noise at higher frequencies (0.32 Hz to 1.08 Hz) and then dividing by the standard deviation of the
346 noise to produce a response metric equivalent to the sensitivity index d'. The metric was
347 computed for each stimulus for every cell so that the cells could be plotted in two different
348 configurations from the literature. In animals M1 and M2, where an L-M isoluminant stimulus, an
349 S-isolating stimulus, and a Luminance stimulus were used, no further analysis was needed, and
350 the data was simply plotted along S vs. L-M axes. In animal M3, since single cone isolating stimuli
351 were used for L, M, and S cones, it was possible to reproduce cone weighting plots such as those
352 in Derrington et. al. [65]. As in that paper, we calculated the cone weights by dividing the response

353 metric by the cone modulation from the stimuli and normalized them all such that the sum of all
354 cone weights added to unity.
355
356 For the spatial frequency data, the temporal speed of the drifting gratings (6 Hz) well exceeded
357 the temporal resolution of the GCaMP6s indicators [70], so cells responding to the grating
358 exhibited an overall increase in fluorescence that saturated after approximately 10-20s. The
359 background level for each cell was calculated as the mean of the first 10s of fluorescence during
360 the adaptation period, while the signal was calculated as the mean of the last 10s of fluorescence
361 recorded during the presentation of the stimulus. The ΔF/F metric commonly used in calcium
362 imaging was calculated for each spatial frequency as the background subtracted from the signal,
363 all divided by the signal at 17 cyc/deg, a spatial frequency producing a robust response across the
364 majority of the cells.
365
366 **Modeling of photoreceptor mosaic and RGC response characteristics**. To connect the measured
367 spatial transfer functions (STFs) to the receptive field (RF) organization of the underlying RGCs,
368 we employed a computational model which simulates optical, spectral, spatial, and temporal
369 components of the AOSLO stimulation apparatus, as well as the animal's optics and cone mosaic
370 structure. The model computes a STF, assuming that that cone signals are pooled by the center
371 and surround mechanisms of an RGC according to a difference of Gaussians (DoG) [91] spatial
372 profile. The parameters of the DoG model and therefore, the actual cone pooling weights, are
373 estimated by minimizing the error between the model and the *in vivo* fluorescence-based STFs.
374 The modeling is implemented within the Imaging Systems Engineering Tools for Biology (ISETBio)
375 software framework [92, 93].
376

A schematic overview of the entire modeling pipeline is depicted in Figure 6. The drifting monochromatic sinusoidal gratings used to measure RGC STFs are modeled as temporal sequences of ISETBio spatial-spectral radiance scenes, where each scene models one frame of the displayed stimulus. The spectral characteristics, spatial extent, and the temporal properties of the AOSLO display subsystem are taken into account in generating the ISETBio scenes. The spectral profile of the monochromatic beam is modeled as Gaussian shaped with a peak at 561 nm and a full-width-half-max (FWHM) bandwidth of 5 nm, and the mean irradiance on the retina is 1.29 mW cm^{-2}. (The power estimate includes absorption by the lens pigment.) The visual stimulus as imaged on the retina has a pixel size of 1.03 µm and its spatial extent in visual angle is 0.7 x 0.7 deg. All sinusoidal gratings are presented with a nominal contrast of 1.0 and are drifted at 6 Hz with a refresh rate of 25.3 Hz for a duration of 666 ms (4 cycles).

The animal's optics during AOSLO-based stimulation are modeled as a diffraction-limited optical system with a small amount of residual defocus blur. The diffraction limit is obtained using the 6.7 mm pupil diameter employed in the experiment assuming a conversion between degrees of visual angle and retinal extent of 199.26 µm/deg. Residual blur in the AOSLO, which might occur due to a slight defocus of the stimulus with respect to the plane of cone inner segments in the retina, is modeled by adjusting the Zernike defocus coefficient used to compute the optical point spread function. The amount of residual blur is not known *a priori* and is estimated as part of model fitting as described below. The temporal sequence of ISETBio spatial-spectral radiance scenes that model of the AOSLO stimulus are passed via the model optical system to generate a corresponding sequence of spatial-spectral retinal irradiance images, which are processed by the cone mosaic model as described next.

401 An ISETBio model of the animal's cone mosaic is generated from cone density maps measured
402 during AOSLO imaging, using an iterative approach described previously [92]. The spatial extent
403 of the cone mosaic is 1.3 x 1.3 deg, with a maximal cone density of 270,200 cones mm^{-2} and with
404 relative L:M:S cone densities of 0.48:0.48:0.04, and without a tritanopic (S-cone free) area at the
405 fovea. Cones are modeled with Gaussian entrance apertures with a characteristic radius equal to
406 $0.204 * \sqrt{2} * D$, where *D* is the inner segment diameter as measured during AOSLO imaging [10].
407 In this cone mosaic model, cone outer segment lengths and macular pigment all vary with
408 eccentricity [92] and the cone quantal efficiencies are based on the Stockman-Sharpe (2000)
409 normalized absorbance measurements [94, 95]. The modeled macular pigment density is from
410 Stockman *et. al.* (1999) [94](http://www.cvrl.org/database/text/maclens/macss.htm) and the
411 modeled lens pigment density is for young subjects (< 20 years) as reported by Pokorny *et. al.*
412 [96].
413
414 To compute a cone's excitation response, the spatial-spectral irradiance impinging on the retina
415 is first spectrally weighted by the product of macular pigment transmittance and by each cone's
416 spectral quantal efficiency, subsequently integrated over wavelength, and spatially integrated
417 over the cone's Gaussian aperture. This excitation response is then integrated over the temporal
418 duration of each stimulus frame (39.5 ms), to estimate the expected excitation events count
419 $E^j(\omega,t)$, for the *j*-th cone in the mosaic, at time *t*, in response to a drifting grating of spatial
420 frequency ω. In these simulations, we do not include Poisson noise in $E^j(\omega,t)$, nor do we introduce
421 positional jitter between the cone mosaic and the retinal stimulus due to eye movements.
422

Assuming that cones are adapted to the mean background irradiance, the excitations response $E^j(\omega,t)$ is converted to contrast response, $R^j(\omega,t)$, by first subtracting the excitation of the cone to the background stimulus E_0^j, and then dividing by it separately for each cone *j,* i.e.:

$$R^j(\omega,t) = \frac{E^j(\omega,t) - E_0^j}{E_0^j}$$

This operation captures an important effect of the photocurrent generation process which converts cone absorption events in the inner segment into ionic currents flowing through the cone outer segment, and which in effect down-regulates the stimulus-induced cone excitation rate with respect to the background cone excitation rate.

Model ganglion cell responses $RGC(\omega,t)$, are computed from the cone contrast responses assuming linear spatial pooling of cone contrast signals by the antagonistic center and surround mechanisms as follows:

$$\begin{aligned} RGC(\omega,t) &= RGC_c(\omega,t) - RGC_s(\omega,t) \\ &= \sum_j W_c^j * R^j(\omega,t) - \sum_j W_s^j * R^j(\omega,t) \end{aligned}$$

where W_c^j and W_r^j are the factors with which the center and surround mechanisms respectively weight the responses $R^j(\omega,t)$. We do not model temporal filtering or delay between center, $RGC_c(\omega,t)$, and surround, $RGC_s(\omega,t)$ responses. Although real RGC responses may be affected by both temporal filtering and a center-surround delay, measurements in this study only recorded amplitude of responses at one temporal frequency with no response phase information, so we cannot meaningfully estimate temporal RGC parameters using the present dataset.

To make computation of cone weights more tractable, we assume that the spatial distribution of cone weights to the center and surround mechanisms have concentric, radially-symmetric Gaussian profiles (Difference of Gaussians, DoG, receptive field model):

$$W_c^j = \begin{cases} k_c * \exp\left[-\left(\frac{d_j}{r_c}\right)^2\right] & (multi - cone\ RF\ center\ model) \\ k_c & (single - cone\ RF\ center\ model) \end{cases}$$

$$W_s^j = k_s * \exp\left[-\left(\frac{d_j}{r_s}\right)^2\right]$$

where d_j is the distance between cone-j and the spatial position of the center mechanism of the model RGC (which is the geometric centroid of the locations of the cones driving the center mechanism). The parameters k_c, k_s, r_c, and r_s, which represent the center and surround peak sensitivities and characteristic radii, respectively, of the DoG RF model are determined by minimizing the root mean squared error (RMSE) between the model-predicted STF, $STF^m(\omega)$, and the measured STF, $STF^{\Delta F/F}(\omega)$, accumulated over all spatial frequencies ω:

$$RMSE = \sqrt{\frac{1}{N} * \sum_{\omega=\omega_1}^{\omega_n} \frac{\beta(\omega)}{\epsilon(\omega)} * [STF^m(\omega) - STF^{\Delta F/F}(\omega)]^2}$$

where $\epsilon(\omega)$ is the standard error of the mean of the $STF^{\Delta F/F}(\omega)$ measurement, and $\beta(\omega)$ is a high-spatial frequency boost factor which linearly increases with spatial frequency from 0.1 to 1.0 over the spatial frequency range 4.7 to 49 c/deg. This boost factor is introduced to emphasize high spatial frequency measurements, the stimulus regime which is maximally informative about the properties of the center mechanism. In some cells, and for certain recording sessions, the measured $STF^{\Delta F/F}(\omega)$ dropped below zero for the lowest spatial frequencies. When this occurs it was accompanied by an apparent overall downward shift in $STF^{\Delta F/F}(\omega)$ across all frequencies, so we assumed that in such cases the background fluorescence was overestimated. To compensate

464 for this, we fit the model to $STF^{\Delta F/F}(\omega)$ – min($STF^{\Delta F/F}(\omega)$) instead of $STF^{\Delta F/F}(\omega)$ in cases where
465 $STF^{\Delta F/F}(\omega)$ dropped below for any spatial frequency. Finally, to reduce the chance of the
466 minimization algorithm getting stuck at a local minimum of the error function, we employ a multi-
467 start minimizer which was run 512 times, keeping the results from the starting point with the
468 minimum RMSE.
469
470 The model-predicted STF, $STF^{m}(\omega)$, is computed by fitting a sinusoidal function to $RGC^{m}(\omega, t)$,
471 $$A(\omega) * \sin\left[2\pi f t - \theta\right]$$
472 where f is set to the temporal frequency of the drifting gratings, and θ, A(ω) are free parameters.
473 At each spatial frequency, the amplitude of the fitted sinusoid, A(ω), is taken as $STF^{m}(\omega)$.
474
475 The model considered four different scenarios: single cone RF centers with and without residual
476 defocus in the AOSLO apparatus, and multiple (1+) cone RF centers with and without AOSLO
477 residual defocus. For each scenario, the model was fit to the STF data of an examined RGC at
478 multiple positions within the cone mosaic and the final model was selected as the one with the
479 minimum RMSE. The multi-position model fitting/selection is performed to take into account
480 variability in cone position due to local inhomogeneities of the cone mosaic and because the exact
481 position of the recorded RGC is only known approximately to reside within the central 40 microns.
482
483 **Results**
484
485 ***In vivo* functional imaging of foveal RGCs.** In this study, optical stimulation of foveal cones elicits
486 the activity of retinal ganglion cells in the living macaque eye. Intravitreal injection of an adeno-
487 associated virus (7m8 or AAV2) with a promotor (ubiquitous CAG or RGC-specific) produced

488 expression of the calcium indicator GCaMP6f [70] in one animal M1 and GCaMP6s [70] in two
489 animals M2 and M3. As previously reported, injections in all three animals produced expression
490 in a ring of RGCs surrounding and radiating out from the foveal avascular zone where the internal
491 limiting membrane is thin [71, 97, 98] (Fig. 1a). Stimuli were presented to the centermost foveal
492 cones while a 488nm imaging laser stimulated fluorescence from GCaMP expressing RGCs in a
493 rectangular area placed either nasally or temporally relative to the cones. Figures 2a-b show the
494 fluorescence response of a single RGC to a simple luminance flicker stimulus in time as well as the
495 resulting Fourier transform, which shows the cell responding primarily at the stimulus frequency.
496 Figure 2c shows that, under our stimulus paradigm, the imaging light did not stimulate foveal
497 cones and confound the recorded functional responses after a 561nm adapting light was
498 presented to the foveal cones. In each animal, hundreds of RGCs were recorded from
499 simultaneously using this stimulus-recording paradigm, using the precision of the AOSLO system
500 to return to the same cells over multiple sessions spanning weeks to months.
501
502 **Reliability and precision of foveal RGC recordings.** Across multiple sessions, RGC cell somas were
503 recorded from over a range of soma locations between 1.2 and 3.5 degrees from the center of
504 the foveal avascular zone (FAZ). When averaging data across multiple experiments, only cells that
505 were visible in all experiments were used. In M3, a followup experiment examining only cone
506 density (Fig. 1b) found the center of the FAZ to be roughly 41 microns inferior and 51 microns
507 nasal from the peak cone density which agrees with the range of data reported from humans [14].
508 Based on detailed receptive field mapping performed by McGregor *et. al.* [16], the cones driving
509 the receptive fields of the cells examined in all three animals are likely to located at eccentricities
510 less than 36 arcmin from the foveal center, or a retinal distance of 120 microns calculated using
511 the primate model eye [99] with the axial lengths of each animal (M1: 17.51 mm, M2: 17.20 mm,

512 M3: 16.56 mm). According to the same mapping, the receptive fields of the innermost cells we
513 recorded from in M3 (Fig. 1c) are likely to be driven by cones found at eccentricities less than 6
514 arcmin, or a retinal distance of 20 microns calculated using the same primate model eye and the
515 axial length of M3 (16.56 mm). Previous functional measurements of RGCs often involved flashed
516 stimuli and marking approximate estimates of soma location or receptive field (RF) eccentricity
517 on fundus images of the retina [e.g. 9, 100], a method that leads to uncertainty about precise
518 locations. In contrast, our imaging method captures photoreceptors, vasculature, and RGC somas
519 in the same field of view, allowing highly accurate measurements of receptive field eccentricity
520 and soma position. Furthermore, unlike in the periphery, foveal RGCs are displaced laterally from
521 their photoreceptor inputs [1, 11, 15, 101], so our paradigm affords the advantage of imaging
522 foveal RGCs without the 488 nm imaging light stimulating foveal cones (Fig. 2c) or the
523 photoreceptor stimuli interfering with the RGC imaging.
524
525 **Chromatic tuning of foveal RGCs.** For functional classification of RGCs with receptive fields at the
526 foveal center, chromatic tuning was measured and averaged across multiple imaging sessions. All
527 visual stimuli delivered to foveal cones were large enough to cover both the FAZ center and the
528 location of maximum cone density and were some 10-60% larger than the cone area servicing
529 even the furthest cells we recorded from, ensuring the best possible chance of recording
530 responses from the maximum number of RGCs.
531
532 Amplitude and phase responses (Fig. 3a-d) to spatially uniform 0.15 Hz or 0.20 Hz flicker
533 modulations that were directed along a combination of L, M, L-M, S, and Luminance directions in
534 color space enabled reliable identification of chromatic tuning of RGCs in all three animals
535 examined. For each cell, the raw fluorescence timecourse was measured in response to each

536 visual stimulus, and the Fourier transform was used to find the cell's response amplitude at the
537 stimulus frequency. The signal-to-noise (SNR) metric used was calculated as the response Fourier
538 amplitude minus the mean amplitudes of higher spatial frequencies (noise) all divided by the
539 standard deviation of the noise. This analysis revealed several functional groups including L-M and
540 M-L opponent cells, ON and OFF S cells, ON and OFF luminance cells, and cells with mixed L-M/S
541 responses. In M3, single cone isolating stimuli were presented to the fovea and the individual
542 cone weights feeding RGCs were calculated similar to what has been done previously in LGN [65]
543 (Fig. 4a-b). This analysis estimates the relative contribution of each cone class to the response of
544 a cell and revealed further diversity of functional groups, including cells with responses to only L
545 or M cones, as well as various S cone connections to cells with L or M cone input that are not L/M
546 opponent.
547
548 **Identification of foveal midget RGCs.** Across all three animals, cells with L-M or M-L chromatic
549 opponent responses (and no response to S-cone stimuli) were identified as putative midget cells.
550 There were a large number of these as can be seen in Figures 3-4: 44% (95% CI true proportion of
551 44±17%) of responsive RGCs closest to the fovea (1.2-1.8 deg soma locations) in M3, 33% (95% CI
552 true proportion of 33±9%) of responsive RGCs over the entire measured range in M3, 72% (95%
553 CI true proportion of 72±8%) of responsive RGCs in M2, and 47% (95% CI true proportion of
554 47±25%) of responsive RGCs in M1. From the literature, it is expected that midget RGCs comprise
555 some 70-90% of foveal cells [20, 50, 101], and the confidence intervals in M1 and M2 contain
556 values in that range. In M3, single cone isolating stimuli were used as detailed in the chromatic
557 stimuli section—it is expected that these stimuli produce lower responses in the classical color-
558 opponent model of midget cells by not driving the center and surround in counterphase as in the
559 isoluminant L-M stimulus used in M1 and M2. There were many cells in M3 (an additional 35% of

560 the closest foveal RGCs, and an additional 32% over the entire measured range) with only a M+/-
561 or L+/- response and no S cone response, and it is possible that some of these cells are chromatic
562 opponent, but that the single cone isolating stimuli produced too small a response from the
563 antagonistic surround in those cases. Based on this uncertainty, we cannot say for sure whether
564 the observed number of putative midget cells in M3 is outside the range of expected values.
565
566 Spatially patterned drifting gratings were also used to probe the spatial frequency response of
567 RGCs and to augment measurements of chromatic tuning (Fig. 5). In M3, at the small field of view
568 focused on the innermost RGCs, a control and fourteen drifting gratings (561 nm, 6 Hz, 4-49c/deg)
569 were used to stimulate foveal cones while the 488 nm imaging light elicited fluorescence from the
570 same GCaMP expressing RGCs shown in Fig. 3d and Fig. 4b. At this temporal frequency, GCaMP
571 could not track modulation and responding cells exhibited a sustained increase in fluorescence in
572 response to photoreceptor stimulation, so a typical ΔF/F metric was calculated for each cell as the
573 change in fluorescence under stimulation divided by the mean fluorescence in response to a
574 grating of 17 c/deg (a spatial frequency with a robust response across the majority of the cells).
575 Most of these putative midget cells at the foveal center in M3 showed two salient features when
576 their spatial frequency response functions were measured: a consistent low frequency cut, and a
577 broadband pass shape with a peak in the higher spatial frequencies from 25-40 cyc/deg.
578
579 Soma size is a useful anatomical measure for distinguishing ganglion cell types and was examined
580 here as a potential correlate with our putative midget cells. RGC soma sizes were measured by
581 two different observers using different methods, but as others have reported, soma sizes did not
582 exhibit bimodalities near the fovea [45] nor distinguish between functional groups identified by

583 chromatic tuning ($p > 0.1$ for comparisons between L/M opponent, S only, Luminance only, and
584 L/M/S cells).
585
586 **Modeling of foveal midget RGCs.**
587 Using the ISETBio modeling approach described previously and schematically depicted in Figure
588 6, we derived estimates of the spatial RF organization from the measured STF data. Results from
589 one RGC are displayed in Figure 7. The RF organization derived from the single-cone RF
590 center/zero residual AOSLO defocus scenario is depicted in the top row. This model predicts a
591 diffuse surround, and results in an STF that deviates systematically from the measured STF at
592 spatial frequencies greater than 30 c/deg. The single-cone RF center/0.067D residual AOSLO
593 defocus scenario predicts a more focal surround and results in an STF that matches the fall-off of
594 the measured STF, resulting in the minimum RMSE across the four examined scenarios. The multi-
595 cone RF center model with zero residual AOSLO defocus model assigns significant weight to a
596 second cone in the center, one horizontally-displaced from the cone with the largest weight. This
597 enlarges the RF center, and as a result makes the STF drop faster as spatial frequency increases
598 beyond the peak spatial frequency, than the STF of the single-cone/zero defocus RF model model.
599 In terms of RMSE, this model performs worse than the single-cone RF center/0.067 defocus
600 model. Moreover, it results in an unusual RF profile, where the RF center is almost the same
601 extent as the RF surround. Finally, the multi-cone RF center model with 0.067D residual defocus
602 model, recruits a vertically-displaced cone in the RF center with a very small weight, so in effect
603 collapses to the single-cone RF center model for the vertical gratings studied here, and results in
604 an STF and RMSE similar to that of the single-cone RF center/0.067D model. Based on these
605 analyses, the most likely RF organization for this cell is a single-cone RF center with some residual
606 defocus in the AOSLO apparatus.

We applied this analysis in 15 RGCs. We obtained similar results in 5/15 cells, with the single-cone RF center/zero residual defocus model having significantly higher RMSE error than the remaining 3 models, accompanied by significantly worse cross validation performance. Of the remaining 3 models, the single-cone RF center/0.067 residual defocus model had either the lowest RMSE or was very close to the model with the lowest RMSE. And again, in those cases the multi-cone RF center with no residual defocus resulted in uncommon RF profiles, whereas the multi-cone RF center/0.067D residual defocus model essentially collapsed into the single-cone RF center/0.067D defocus model.

In the remaining 10/15 cells, the four examined models had similar RMSE error and cross-validation performance. One example of these cells can be seen in Figure 8. Note that all scenarios result in fits of similar RMSE. The 2 scenarios with zero residual defocus (rows 1 and 3) predict a RF with a large surround, whereas the 2 scenarios with 0.067D residual defocus (rows 2 and 4) predict a RF with a much more focal surround. Also note that the two multi-cone RF center scenarios (rows 3 and 4), assign very small weights to the non-dominant center cones, essentially collapsing to their single-cone RF center counterparts.

A notable observation of the STFs in our population of foveal RGCs is the very large amount of low-spatial frequency attenuation. Such observations are not typical of midget ganglion cells reported in other in-vivo studies [9]. The question then arises as to whether these very foveal cells have distinctively different RF organization from the less-foveal cells reported in other studies, or whether the underlying RF organization is similar, but the measured data differ between the 2 types of studies simply because of differences in the optical systems involved. To address this, we

conducted additional simulations, in which we simulated the STFs of model cells using an estimate of the animal's physiological optics (as characterized by wavefront aberration measurements performed on the same animal). For these simulations we constructed synthetic RFs based on the cone pooling weights derived by the best fitting model to the AOSLO-measurements. Results of this analysis are displayed in Figure 9. Here, gray disks and black lines depict the AOSLO STF data obtained under a 6.7 mm pupil, and the ISETBio best fit model to these data. Red disks depict the STFs computed using the derived RF model and the animal's physiological optics for a 2.5 mm pupil. These data would be representative of the STFs measured in traditional in-vivo experiments. Note that for all cells, there is a clear shift of peak sensitivity toward lower spatial frequencies, accompanied by a reduction in low-spatial frequency attenuation, and the resulting STFs are more reminiscent of traditionally mapped STFs.

To make our results more quantitative, we fitted the DoG model to these data, and we contrasted the derived DoG parameters to those reported by Cronner & Kaplan. The results of this analysis are shown in Figure 10, which depicts three key characteristics of this model: the ratio of center-to-surround peak sensitivities (left column), the ratio of surround-to-center characteristic radii (middle column) and the ratios of surround-to-center integrated sensitivities (right column). Data shown in the top row were obtained under diffraction-limited optics in the population of the 15 foveal cells recorded in M3, whereas data shown in the middle row were obtained by simulating physiological optical conditions using the animal's own wavefront aberration optics, again in the same population of the 15 foveal cells. The bottom row depicts data from the Croner&Kaplan '94 study, which was conducted in a population of animals with RGCs located at a wide range of eccentricities under physiological optics. We see that compared to the physiological optics derived data, under diffraction-limited optics, the Kc/Ks ratios are significantly smaller (median of 6.2 vs 16.4), whereas the derived Rs/Rc ratios are somewhat larger (median of 4.6 vs 3.4). The two factors combine in

such a way that under diffraction-limited optics the integrated sensitivity of the surround is on average 3.3 stronger than the integrated sensitivity of the center. In sharp contrast, under physiological optics, the median integrated sensitivity of the RF surround is 0.7 times the sensitivity of the RF center, both in our M3 population with optics added back in and in the population of Croner&Kaplan. This change in center/surround balance is purely a manifestation of the differential effect of optics (black like at the inset) on the center MTF (red line) as compared to the surround MTF (blue line), which transforms the MTF of RGCs (purple lines) from strongly bandpass, under diffraction-limited optics, to weakly bandpass under physiological optics.

Discussion

In this study, we repeatedly imaged *in vivo* the same RGCs serving the foveal center in three animals, returning to the same locations each time. Spatially uniform chromatic visual stimuli enabled the identification of L/M opponent cells which were further interrogated with drifting gratings of various spatial frequencies in one animal. The L/M opponency and high spatial frequency responses of these cells identifies them as candidate midget cells, and our modelling is consistent with the hypothesis that these cells have single cone center inputs and are specialized to maintain the resolution of the photoreceptor mosaic.

Measuring the precise location of cells from the foveal center. In our data, the foveal avascular zone was used as the 'center' measurement of the fovea out of convenience. When imaging both the foveal cones and the RGCs as in our stimulation paradigm (Fig. 1a), the resolution is not sufficient to accurately identify the very smallest foveal cones, so the location of maximum photoreceptor density must be obtained from a separate experiment (Fig. 1b). Another common method of locating the fovea is the preferred retinal locus of fixation (PRL), which is not possible to measure using our method since the animals are anesthetized and cannot fixate or

accommodate. The center of the ganglion cells surrounding the fovea is also sometimes used, but this measure is highly correlated with the center of the FAZ [11, 102]. Others have characterized the precise nature of the relationship between these measures [14], and as noted in the results, our measurements of the difference between the center of the FAZ and the location of maximum cone density in M3 are in agreement with that literature. In any case, the difference in identification of the 'foveal center' is not large enough under our method to affect the conclusion that, using the mapping of McGregor *et. al.* [16], the receptive fields we examined are located near the very center of the fovea.

The role of midgets in foveal vision. Among the putative midgets from M3 (Fig. 5), there was some variability among the responses to spatial frequencies. Especially among those cells from M3 closest to the foveal center, there were two salient features: firstly, that several cells possess low frequency responses and falloffs characteristic of little or absent inhibition from the surround, and secondly, that most of the cells are tuned to quite high spatial frequencies. Previous studies examining parvocellular neurons in the lateral geniculate nucleus (LGN) serving the central five degrees of retina found an average of 4.57±2.75 cyc/deg as the peak spatial frequency response [67], and other studies in the retina itself found parvocellular cells in the central five degrees to have a peak spatial frequency response around 3 cyc/deg [9], whereas our cells mostly have peak responses from 25-40 cyc/deg. However, these previous studies relied on presenting stimuli through the animals' optics, whereas the adaptive optics method we use approaches near diffraction-limited stimulus presentation. We thus measure foveal RGCs not only closer to the foveal center but also with diminished optical blur in the *in vivo* retina compared to previous studies. Indeed, current modeling of the response curves such as those in Figures 5,7-8 that adds back in ocular aberrations shows that the response curves shift toward lower and lower

705 frequencies (Fig. 9-10) and exhibit the more band-pass structure observed in previous studies [9,
706 67], suggesting that our data are consistent with the responses from those studies when the
707 optics are re-introduced to our measurements.
708
709 Putative midget cells serving the very central fovea with lower spatial frequency response peaks
710 (4-15 cyc/deg) comprised a small fraction of the responsive chromatic opponent cells (3 out of 15
711 in M3) and tended to be noisier than average but were all repeatably far more responsive to low
712 spatial frequencies with difference of gaussian fits suggesting that the centers were comprised of
713 a single cone on average with small or insignificant inhibition from the surround of these cells.
714 Surprisingly, this is closer to the classical expectation of midget cells**,** which are thought to be
715 dominated by center responses some 10-1000x stronger than those of the surround [9] at the
716 fovea in order to facilitate the 'double-duty' of transferring both achromatic and chromatic vision
717 across a wide range of spatial frequencies but with peaks close to the psychophysical peak
718 sensitivity of 3-5 cyc/deg [103]. Further study on these low-frequency L/M chromatic opponent
719 cells will confirm if they exhibit any other physiological differences or if they belong to one or
720 more of several midget subtypes as others have postulated to exist [47, 58].
721
722 Of the remaining 12 chromatic opponent L/M RGCs serving the very central fovea, all of them
723 possessed strong inhibition from the surround and peak spatial responses between 25-40
724 cyc/deg, far higher than was ever measured through the optics as confirmed by our modeling. We
725 posit that since the fovea is specialized for high acuity vision, it must be capable of extracting high
726 spatial frequency information from natural scenes which are known to follow a $1/f^2$ law [104] and
727 be dominated by low frequency information. Indeed, our modeling suggests that the natural
728 ocular aberrations further reduce the peak spatial frequency from only diffractive effects by a

729 factor of three or more which means that high spatial frequency information is greatly reduced
730 through ocular transmission. Thus, to extract meaningful high spatial frequency information from
731 natural scenes through the eye's native optics, detectors that preserve information at the
732 resolution of the photoreceptor mosaic are required. It seems highly likely that the putative
733 midget cells shown in Figures 5,7 are responsible for this resolution, as they have responses
734 consistent with single cone receptive field centers. Our data are consistent with the hypothesis
735 that there are subtypes of foveal midget ganglion cell types responsible for different regions of
736 the spatial frequency spectrum and that all or most of midget cells produce strong chromatic
737 responses, consistent with either the double-duty hypothesis or the hypothesis of subtypes of
738 midgets responsible solely for either chromatic or achromatic vision [58]. There is also evidence
739 that parasol ganglion cells respond weakly to L/M chromatic modulation [105], so we cannot rule
740 out at this time the possibility that a small number of these putative midget cells are actually
741 parasol cells.
742
743 **Modeling foveal RGCs.** There are two reasons it is difficult to differentiate between single and
744 multi-cone models from our data. First, for technical reasons, our present measurements did not
745 extend to high spatial frequencies where the different models would have more clearly different
746 predictions. Second, there was inter-session variability in the measured STFs, which decreases the
747 power of the data to identify a model. In future experiments, we will increase the power of the
748 data by (i) extending the range of spatial frequencies examined and (ii) testing multiple grating
749 orientations. The modeling has the capability to add in a subject's PSF (including the measured
750 wavefront aberrations from M3) to predict responses to stimuli presented through the natural
751 (non AO-corrected) optics. The robust nature of the entire simulation allows for any cone density

752 profile or PSF to be substituted in the model so that the simulation can be generalized for
753 population data or be tailored to individual subjects as it has been here for M3.
754
755 **S-cone mediated color vision in the fovea.** As shown in Figures 3-4, cells with either S cone input
756 without L/M chromatic opponency (pure) or S cone input on top of L/M chromatic opponency
757 (mixed) were observed in each animal: 40% of responsive cells exhibited pure responses and 7%
758 mixed in M1, 9% pure and 14% mixed in M2, 16% pure and 3% mixed in the entirety of M3, while
759 no consistent S cone responses were recorded from the centermost foveal cells in M3. Other than
760 in M1 where the sample size was only 15 cells, these numbers are consistent with the expected S
761 cone density of approximately 10% across primate fovea [106] and known reduction of S cone
762 density at the very center of the primate fovea [8, 15]. Others have reported additional subtypes
763 of midget RGCs with S cone input or even that midgets may indiscriminately contact S cones along
764 with L and M cones in the surround [17, 47, 58]. Our current data set has no repeatable S cone
765 responses at the innermost foveal edge of M3 where RGCs are optically isolated, so we cannot
766 currently rule out that the mixed cells we measure are partially or fully the product of optical
767 crosstalk.
768
769 **Putative parasol cells at the fovea.** As shown in Figures 3-4, cells with no chromatic responses
770 but only a L+M or -L-M luminance response were recorded from each of the three animals: 7% of
771 responsive cells in M1, 4% in M2, 15% in the entirety of M3 and 20% of the centermost foveal
772 cells in M3, consistent with expected proportions of parasol ganglion cells, which are known to
773 mediate achromatic vision [20]. Simple modeling based on hexagonal packing of cones and
774 random wiring of 6 cones to midget surrounds suggests that approximately 10% of midget cells
775 could be dominated by a single cone type and appear achromatic. It is probable then that some

776 of these achromatic cells are midgets but that most of them are candidate parasol cells, though
777 at this time we cannot make that distinction for an individual cell. The spatial frequency response
778 properties of these cells were even more varied than the chromatic opponent cells, suggesting
779 that they might be responsible for a wide range of achromatic or even temporal vision properties
780 that complement the dominant midget system. As noted in the results, we have not found
781 significant differences between soma sizes of putative foveal parasols and midgets, so additional
782 anatomical information such as histological studies may be required in the future to confirm
783 functional designations.
784
785 **Acknowledgments**
786
787 The authors would like to thank Amber Walker for performing animal anesthesia and monitoring
788 during imaging, , Max Snodderly for assistance with estimating the effect of macular pigment,
789 Charles Granger for optical alignment assistance, Daniel Guarino and Martin Gira for maintaining
790 the stereotaxic cart and other electronic components, as well as Aby Joseph, Jennifer Hunter, and
791 Jesse Schallek for data analysis suggestions. We thank the vector core at the Perelman School of
792 Medicine, University of Pennsylvania and the Genetically-Encoded Neuronal Indicator and
793 Effector (GENIE) Project and the Janelia Research Campus of the Howard Hughes Medical
794 Institute, specifically Vivek Jayaraman, Ph.D., Douglas S. Kim, Ph.D., Loren L. Looger, Ph.D., and
795 Karel Svoboda, Ph.D.
796
797 **References**

798 1. Schein SJ. Anatomy of macaque fovea and spatial densities of neurons in foveal
799 representation. J Comp Neurol. 1988;269(4):479-505. Epub 1988/03/22. doi:
800 10.1002/cne.902690403. PubMed PMID: 3372725.
801 2. Wassle H, Grunert U, Rohrenbeck J, Boycott BB. Cortical magnification factor and the
802 ganglion cell density of the primate retina. Nature. 1989;341(6243):643-6. Epub 1989/10/19.
803 doi: 10.1038/341643a0. PubMed PMID: 2797190.
804 3. Wassle H, Grunert U, Rohrenbeck J, Boycott BB. Retinal ganglion cell density and cortical
805 magnification factor in the primate. Vision Res. 1990;30(11):1897-911. Epub 1990/01/01.
806 PubMed PMID: 2288097.
807 4. De Monasterio FM, Gouras P. Functional properties of ganglion cells of the rhesus
808 monkey retina. J Physiol. 1975;251(1):167-95. Epub 1975/09/01. doi:
809 10.1113/jphysiol.1975.sp011086. PubMed PMID: 810576; PubMed Central PMCID:
810 PMCPMC1348381.
811 5. Derrington AM, Lennie P. Spatial and temporal contrast sensitivities of neurones in
812 lateral geniculate nucleus of macaque. J Physiol. 1984;357:219-40. Epub 1984/12/01. doi:
813 10.1113/jphysiol.1984.sp015498. PubMed PMID: 6512690; PubMed Central PMCID:
814 PMCPMC1193256.
815 6. Watanabe M, Rodieck RW. Parasol and midget ganglion cells of the primate retina. J
816 Comp Neurol. 1989;289(3):434-54. Epub 1989/11/15. doi: 10.1002/cne.902890308. PubMed
817 PMID: 2808778.
818 7. Kolb H, Dekorver L. Midget ganglion cells of the parafovea of the human retina: a study
819 by electron microscopy and serial section reconstructions. J Comp Neurol. 1991;303(4):617-36.
820 Epub 1991/01/22. doi: 10.1002/cne.903030408. PubMed PMID: 1707423.
821 8. Hendrickson A. A morphological comparison of foveal development in man and monkey.
822 Eye (Lond). 1992;6 (Pt 2):136-44. Epub 1992/01/01. doi: 10.1038/eye.1992.29. PubMed PMID:
823 1624035.
824 9. Croner LJ, Kaplan E. Receptive fields of P and M ganglion cells across the primate retina.
825 Vision Res. 1995;35(1):7-24. Epub 1995/01/01. doi: 10.1016/0042-6989(94)e0066-t. PubMed
826 PMID: 7839612.
827 10. McMahon MJ, Lankheet MJ, Lennie P, Williams DR. Fine structure of parvocellular
828 receptive fields in the primate fovea revealed by laser interferometry. J Neurosci.
829 2000;20(5):2043-53. Epub 2000/02/24. PubMed PMID: 10684905.
830 11. Hendrickson A. Organization of the Adult Primate Fovea. In: Penfold PL, Provis JM,
831 editors. Macular Degeneration: Springer Berlin Heidelberg; 2005.
832 12. Yin L, Masella B, Dalkara D, Zhang J, Flannery JG, Schaffer DV, et al. Imaging light
833 responses of foveal ganglion cells in the living macaque eye. J Neurosci. 2014;34(19):6596-605.
834 Epub 2014/05/09. doi: 10.1523/jneurosci.4438-13.2014. PubMed PMID: 24806684; PubMed
835 Central PMCID: PMCPMC4012315.
836 13. Sinha R, Hoon M, Baudin J, Okawa H, Wong ROL, Rieke F. Cellular and Circuit
837 Mechanisms Shaping the Perceptual Properties of the Primate Fovea. Cell. 2017;168(3):413-
838 26.e12. Epub 2017/01/28. doi: 10.1016/j.cell.2017.01.005. PubMed PMID: 28129540; PubMed
839 Central PMCID: PMCPMC5298833.
840 14. Wilk MA, Dubis AM, Cooper RF, Summerfelt P, Dubra A, Carroll J. Assessing the spatial
841 relationship between fixation and foveal specializations. Vision Research. 2017;132:53-61. doi:
842 https://doi.org/10.1016/j.visres.2016.05.001.

15. Bringmann A, Syrbe S, Gorner K, Kacza J, Francke M, Wiedemann P, et al. The primate fovea: Structure, function and development. Prog Retin Eye Res. 2018;66:49-84. Epub 2018/04/03. doi: 10.1016/j.preteyeres.2018.03.006. PubMed PMID: 29609042.
16. McGregor JE, Yin L, Yang Q, Godat T, Huynh KT, Zhang J, et al. Functional architecture of the foveola revealed in the living primate. PLoS One. 2018;13(11):e0207102. Epub 2018/11/30. doi: 10.1371/journal.pone.0207102. PubMed PMID: 30485298; PubMed Central PMCID: PMCPMC6261564 following competing interests: DRW and WHM receive funding from the National Eye Institute. DRW receives additional funding from The Arnold and Mabel Beckman Foundation and WHM receives funding from Research to Prevent Blindness as detailed in the Financial Disclosure statement. DRW has patents with the University of Rochester for adaptive optics imaging of the retina: US patent #6,199,986 "Rapid, automatic measurement of the eye's wave aberration". US patent #6,264,328 "Wavefront sensor with off-axis illumination" and US patent 6,338,559 "Apparatus and method for improving vision and retinal imaging". QY has patents with the University of Rochester, Canon Inc. and the University of Montana, for image stabilization algorithms: US patent #9,226,656: "Real-time optical and digital image stabilization for adaptive optics scanning ophthalmoscopy", US patent # 9,406,133: "System and method for real-time image registration", US patent #: 9,485,383, "Imaging based correction of distortion from a scanner" and US patent #: 9,454,084, "Light source modulation for a scanning microscope". Additionally QY has undertaken consultancy work for Oculus VR and Boston Micromachine Corporation. This does not alter our adherence to PLOS ONE policies on sharing data and materials.
17. Thoreson WB, Dacey DM. Diverse Cell Types, Circuits, and Mechanisms for Color Vision in the Vertebrate Retina. Physiol Rev. 2019;99(3):1527-73. Epub 2019/05/30. doi: 10.1152/physrev.00027.2018. PubMed PMID: 31140374; PubMed Central PMCID: PMCPMC6689740.
18. Dacey DM. The mosaic of midget ganglion cells in the human retina. J Neurosci. 1993;13(12):5334-55. Epub 1993/12/01. PubMed PMID: 8254378.
19. Dacey DM. Primate retina: cell types, circuits and color opponency. Prog Retin Eye Res. 1999;18(6):737-63. Epub 1999/10/26. doi: 10.1016/s1350-9462(98)00013-5. PubMed PMID: 10530750.
20. Dacey DM. Origins of Perception: Retinal Ganglion Cell Diversity and the Creation of Parallel Visual Pathways. In: Gazzaniga MS, editor. The Cognitive Neurosciences: The MIT Press; 2004. p. 281-302.
21. Leventhal AG, Rodieck RW, Dreher B. Retinal ganglion cell classes in the Old World monkey: morphology and central projections. Science. 1981;213(4512):1139-42. Epub 1981/09/04. doi: 10.1126/science.7268423. PubMed PMID: 7268423.
22. Perry VH, Cowey A. Retinal ganglion cells that project to the superior colliculus and pretectum in the macaque monkey. Neuroscience. 1984;12(4):1125-37. Epub 1984/08/01. doi: 10.1016/0306-4522(84)90007-1. PubMed PMID: 6483194.
23. Perry VH, Oehler R, Cowey A. Retinal ganglion cells that project to the dorsal lateral geniculate nucleus in the macaque monkey. Neuroscience. 1984;12(4):1101-23. Epub 1984/08/01. doi: 10.1016/0306-4522(84)90006-x. PubMed PMID: 6483193.
24. Kaplan E, Shapley RM. The primate retina contains two types of ganglion cells, with high and low contrast sensitivity. Proceedings of the National Academy of Sciences of the United States of America. 1986;83(8):2755-7. Epub 1986/04/01. doi: 10.1073/pnas.83.8.2755. PubMed PMID: 3458235; PubMed Central PMCID: PMCPMC323379.

889 25. Perry VH, Silveira LCL. Functional lamination in the ganglion cell layer of the macaque's
890 retina. Neuroscience. 1988;25(1):217-23. doi: https://doi.org/10.1016/0306-4522(88)90020-6.
891 26. Dacey DM, Petersen MR. Dendritic field size and morphology of midget and parasol
892 ganglion cells of the human retina. Proceedings of the National Academy of Sciences of the
893 United States of America. 1992;89(20):9666-70. doi: 10.1073/pnas.89.20.9666. PubMed PMID:
894 1409680.
895 27. Grunert U, Greferath U, Boycott BB, Wassle H. Parasol (P alpha) ganglion-cells of the
896 primate fovea: immunocytochemical staining with antibodies against GABAA-receptors. Vision
897 Res. 1993;33(1):1-14. Epub 1993/01/01. PubMed PMID: 8383899.
898 28. Dacey DM. Morphology of a small-field bistratified ganglion cell type in the macaque
899 and human retina. Vis Neurosci. 1993;10(6):1081-98. Epub 1993/11/01. doi:
900 10.1017/s0952523800010191. PubMed PMID: 8257665.
901 29. Dacey DM, Lee BB. The 'blue-on' opponent pathway in primate retina originates from a
902 distinct bistratified ganglion cell type. Nature. 1994;367(6465):731-5. Epub 1994/02/24. doi:
903 10.1038/367731a0. PubMed PMID: 8107868.
904 30. Graham DM, Wong KY. Melanopsin-expressing, Intrinsically Photosensitive Retinal
905 Ganglion Cells (ipRGCs). In: Kolb H, Fernandez E, Nelson R, editors. Webvision: The Organization
906 of the Retina and Visual System. Salt Lake City (UT)1995.
907 31. Dacey DM. Circuitry for color coding in the primate retina. Proceedings of the National
908 Academy of Sciences of the United States of America. 1996;93(2):582-8. Epub 1996/01/23. doi:
909 10.1073/pnas.93.2.582. PubMed PMID: 8570599; PubMed Central PMCID: PMCPMC40095.
910 32. Lee BB. Receptive field structure in the primate retina. Vision Research. 1996;36(5):631-
911 44. doi: https://doi.org/10.1016/0042-6989(95)00167-0.
912 33. Calkins DJ, Tsukamoto Y, Sterling P. Microcircuitry and mosaic of a blue-yellow ganglion
913 cell in the primate retina. J Neurosci. 1998;18(9):3373-85. Epub 1998/05/09. PubMed PMID:
914 9547245; PubMed Central PMCID: PMCPMC6792640.
915 34. Chichilnisky EJ, Baylor DA. Receptive-field microstructure of blue-yellow ganglion cells in
916 primate retina. Nat Neurosci. 1999;2(10):889-93. Epub 1999/09/24. doi: 10.1038/13189.
917 PubMed PMID: 10491609.
918 35. Telkes I, Distler C, Hoffmann KP. Retinal ganglion cells projecting to the nucleus of the
919 optic tract and the dorsal terminal nucleus of the accessory optic system in macaque monkeys.
920 Eur J Neurosci. 2000;12(7):2367-75. Epub 2000/08/18. doi: 10.1046/j.1460-9568.2000.00133.x.
921 PubMed PMID: 10947815.
922 36. Dacey DM, Liao HW, Peterson BB, Robinson FR, Smith VC, Pokorny J, et al. Melanopsin-
923 expressing ganglion cells in primate retina signal colour and irradiance and project to the LGN.
924 Nature. 2005;433(7027):749-54. Epub 2005/02/18. doi: 10.1038/nature03387. PubMed PMID:
925 15716953.
926 37. Calkins DJ, Sterling P. Microcircuitry for two types of achromatic ganglion cell in primate
927 fovea. J Neurosci. 2007;27(10):2646-53. Epub 2007/03/09. doi: 10.1523/JNEUROSCI.4739-
928 06.2007. PubMed PMID: 17344402; PubMed Central PMCID: PMCPMC6672494.
929 38. Petrusca D, Grivich MI, Sher A, Field GD, Gauthier JL, Greschner M, et al. Identification
930 and characterization of a Y-like primate retinal ganglion cell type. J Neurosci.
931 2007;27(41):11019-27. Epub 2007/10/12. doi: 10.1523/jneurosci.2836-07.2007. PubMed PMID:
932 17928443.
933 39. Field GD, Sher A, Gauthier JL, Greschner M, Shlens J, Litke AM, et al. Spatial Properties
934 and Functional Organization of Small Bistratified Ganglion Cells in Primate Retina. The Journal of
935 Neuroscience. 2007;27(48):13261-72. doi: 10.1523/jneurosci.3437-07.2007.

936 40. Crook JD, Peterson BB, Packer OS, Robinson FR, Gamlin PD, Troy JB, et al. The smooth
937 monostratified ganglion cell: evidence for spatial diversity in the Y-cell pathway to the lateral
938 geniculate nucleus and superior colliculus in the macaque monkey. J Neurosci.
939 2008;28(48):12654-71. Epub 2008/11/28. doi: 10.1523/jneurosci.2986-08.2008. PubMed PMID:
940 19036959; PubMed Central PMCID: PMCPMC2778055.
941 41. Percival KA, Martin PR, Grunert U. Organisation of koniocellular-projecting ganglion cells
942 and diffuse bipolar cells in the primate fovea. Eur J Neurosci. 2013;37(7):1072-89. Epub
943 2013/01/15. doi: 10.1111/ejn.12117. PubMed PMID: 23311464.
944 42. Crook JD, Packer OS, Troy JB, Dacey DM. Synaptic Mechanisms of Color and Luminance
945 Coding: Rediscovering the X-Y-cell dichotomy in primate retinal ganglion cels. . In: Werner JS,
946 Chalupa LM, editors. The New Visual Neurosciences: The MIT Press; 2013. p. 123-44.
947 43. Puller C, Manookin MB, Neitz J, Rieke F, Neitz M. Broad thorny ganglion cells: a
948 candidate for visual pursuit error signaling in the primate retina. J Neurosci. 2015;35(13):5397-
949 408. Epub 2015/04/04. doi: 10.1523/jneurosci.4369-14.2015. PubMed PMID: 25834063;
950 PubMed Central PMCID: PMCPMC4381007.
951 44. Liao HW, Ren X, Peterson BB, Marshak DW, Yau KW, Gamlin PD, et al. Melanopsin-
952 expressing ganglion cells on macaque and human retinas form two morphologically distinct
953 populations. J Comp Neurol. 2016;524(14):2845-72. Epub 2016/03/15. doi: 10.1002/cne.23995.
954 PubMed PMID: 26972791; PubMed Central PMCID: PMCPMC4970949.
955 45. Liu Z, Kurokawa K, Zhang F, Lee JJ, Miller DT. Imaging and quantifying ganglion cells and
956 other transparent neurons in the living human retina. Proceedings of the National Academy of
957 Sciences of the United States of America. 2017;114(48):12803-8. Epub 2017/11/16. doi:
958 10.1073/pnas.1711734114. PubMed PMID: 29138314; PubMed Central PMCID:
959 PMCPMC5715765.
960 46. Peng YR, Shekhar K, Yan W, Herrmann D, Sappington A, Bryman GS, et al. Molecular
961 Classification and Comparative Taxonomics of Foveal and Peripheral Cells in Primate Retina. Cell.
962 2019;176(5):1222-37 e22. Epub 2019/02/05. doi: 10.1016/j.cell.2019.01.004. PubMed PMID:
963 30712875; PubMed Central PMCID: PMCPMC6424338.
964 47. Wool LE, Packer OS, Zaidi Q, Dacey DM. Connectomic Identification and Three-
965 Dimensional Color Tuning of S-OFF Midget Ganglion Cells in the Primate Retina. J Neurosci.
966 2019;39(40):7893-909. Epub 2019/08/14. doi: 10.1523/JNEUROSCI.0778-19.2019. PubMed
967 PMID: 31405926; PubMed Central PMCID: PMCPMC6774400.
968 48. Rhoades CE, Shah NP, Manookin MB, Brackbill N, Kling A, Goetz G, et al. Unusual
969 Physiological Properties of Smooth Monostratified Ganglion Cell Types in Primate Retina.
970 Neuron. 2019;103(4):658-72 e6. Epub 2019/06/23. doi: 10.1016/j.neuron.2019.05.036. PubMed
971 PMID: 31227309; PubMed Central PMCID: PMCPMC6817368.
972 49. Dacey DM, Kim YJ, Packer OS, Detwiler PB. ON-OFF direction selective ganglion cells in
973 macaque monkey retina are tracer-coupled to an ON-OFF direction selective amacrine cell type.
974 Investigative Ophthalmology & Visual Science. 2019;60(9):5280-.
975 50. Kim US, Mahroo OA, Mollon JD, Yu-Wai-Man P. Retinal Ganglion Cells—Diversity of Cell
976 Types and Clinical Relevance. Frontiers in Neurology. 2021;12(635). doi:
977 10.3389/fneur.2021.661938.
978 51. Grünert U, Martin PR. Cell types and cell circuits in human and non-human primate
979 retina. Progress in Retinal and Eye Research. 2020;78:100844. doi:
980 https://doi.org/10.1016/j.preteyeres.2020.100844.
981 52. Valois RLD, Jacobs GH. Primate Color Vision. Science. 1968;162(3853):533-40. doi:
982 doi:10.1126/science.162.3853.533.

53. Calkins DJ, Sterling P. Evidence that Circuits for Spatial and Color Vision Segregate at the First Retinal Synapse. Neuron. 1999;24(2):313-21. doi: 10.1016/S0896-6273(00)80846-6.
54. Rodieck RW. Which Cells Code for Color? In: Valberg A, Lee BB, editors. From Pigments to Perception: Advances in Understanding Visual Processes. Boston, MA: Springer US; 1991. p. 83-93.
55. Gegenfurtner KR, Kiper DC. Color vision. Annu Rev Neurosci. 2003;26:181-206. Epub 2003/02/08. doi: 10.1146/annurev.neuro.26.041002.131116. PubMed PMID: 12574494.
56. Crook JD, Dacey DM. Circuitry and receptive field structure underlying 'double duty' performance by midget ganglion cells. Journal of Vision. 2010;10(15):5-. doi: 10.1167/10.15.5.
57. Crook JD, Packer OS, Manookin MB, Dacey DM. Distinct Spatio-chromatic Receptive Field Structure Mediates Red-green Opponency And High Achromatic Contrast Sensitivity In Primate Midget Ganglion Cells. Investigative Ophthalmology & Visual Science. 2011;52(14):3905-.
58. Patterson SS, Neitz M, Neitz J. Reconciling Color Vision Models With Midget Ganglion Cell Receptive Fields. Front Neurosci. 2019;13:865. Epub 2019/09/03. doi: 10.3389/fnins.2019.00865. PubMed PMID: 31474825; PubMed Central PMCID: PMCPMC6707431.
59. Lee BB, Martin PR, Valberg A. Sensitivity of macaque retinal ganglion cells to chromatic and luminance flicker. The Journal of physiology. 1989;414:223-43. doi: 10.1113/jphysiol.1989.sp017685. PubMed PMID: 2607430.
60. Lee BB, Pokorny J, Smith VC, Martin PR, Valberg A. Luminance and chromatic modulation sensitivity of macaque ganglion cells and human observers. J Opt Soc Am A. 1990;7(12):2223-36. Epub 1990/12/01. doi: 10.1364/josaa.7.002223. PubMed PMID: 2090801.
61. Soto F, Hsiang J-C, Rajagopal R, Piggott K, Harocopos GJ, Couch SM, et al. Efficient Coding by Midget and Parasol Ganglion Cells in the Human Retina. Neuron. 2020;107(4):656-66.e5. doi: https://doi.org/10.1016/j.neuron.2020.05.030.
62. Brackbill N, Rhoades C, Kling A, Shah NP, Sher A, Litke AM, et al. Reconstruction of natural images from responses of primate retinal ganglion cells. eLife. 2020;9:e58516. doi: 10.7554/eLife.58516. PubMed PMID: 33146609.
63. Calkins DJ, Schein SJ, Tsukamoto Y, Sterling P. M and L cones in macaque fovea connect to midget ganglion cells by different numbers of excitatory synapses. Nature. 1994;371(6492):70-2. doi: 10.1038/371070a0.
64. Kaas JH, Guillery RW, Allman JM. Some Principles of Organization in the Dorsal Lateral Geniculate Nucleus; pp. 253–267. Brain, Behavior and Evolution. 1972;6(1-6):253-67. doi: 10.1159/000123713.
65. Derrington AM, Krauskopf J, Lennie P. Chromatic mechanisms in lateral geniculate nucleus of macaque. J Physiol. 1984;357:241-65. Epub 1984/12/01. doi: 10.1113/jphysiol.1984.sp015499. PubMed PMID: 6512691; PubMed Central PMCID: PMCPMC1193257.
66. Solomon SG, Peirce JW, Dhruv NT, Lennie P. Profound contrast adaptation early in the visual pathway. Neuron. 2004;42(1):155-62. Epub 2004/04/07. doi: 10.1016/s0896-6273(04)00178-3. PubMed PMID: 15066272.
67. Levitt JB, Schumer RA, Sherman SM, Spear PD, Movshon JA. Visual response properties of neurons in the LGN of normally reared and visually deprived macaque monkeys. J Neurophysiol. 2001;85(5):2111-29. Epub 2001/05/16. doi: 10.1152/jn.2001.85.5.2111. PubMed PMID: 11353027.

1029 68. Gray DC, Merigan W, Wolfing JI, Gee BP, Porter J, Dubra A, et al. In vivo fluorescence
1030 imaging of primate retinal ganglion cells and retinal pigment epithelial cells. Optics express.
1031 2006;14(16):7144-58. Epub 2006/08/07. doi: 10.1364/oe.14.007144. PubMed PMID: 19529085.
1032 69. Yin L, Geng Y, Osakada F, Sharma R, Cetin AH, Callaway EM, et al. Imaging light
1033 responses of retinal ganglion cells in the living mouse eye. J Neurophysiol. 2013;109(9):2415-21.
1034 Epub 2013/02/15. doi: 10.1152/jn.01043.2012. PubMed PMID: 23407356; PubMed Central
1035 PMCID: PMCPMC3652215.
1036 70. Chen T-W, Wardill TJ, Sun Y, Pulver SR, Renninger SL, Baohan A, et al. Ultrasensitive
1037 fluorescent proteins for imaging neuronal activity. Nature. 2013;499(7458):295-300. doi:
1038 10.1038/nature12354. PubMed PMID: 23868258.
1039 71. Yin L, Greenberg K, Hunter JJ, Dalkara D, Kolstad KD, Masella BD, et al. Intravitreal
1040 injection of AAV2 transduces macaque inner retina. Invest Ophthalmol Vis Sci. 2011;52(5):2775-
1041 83. Epub 2011/02/12. doi: 10.1167/iovs.10-6250. PubMed PMID: 21310920; PubMed Central
1042 PMCID: PMCPMC3088562.
1043 72. Delori FC, Webb RH, Sliney DH. Maximum permissible exposures for ocular safety (ANSI
1044 2000), with emphasis on ophthalmic devices. J Opt Soc Am A. 2007;24(5):1250-65. doi:
1045 10.1364/JOSAA.24.001250.
1046 73. Schulmeister K. The upcoming new editions of IEC 60825-1 and ANSI Z136.1 – Examples
1047 on impact for classification and exposure limits. International Laser Safety Conference.
1048 2013;2013(1):330-7. doi: 10.2351/1.5056809.
1049 74. Rockwell B, Thomas R, Zimmerman S. Updates to the ANSI Z136.1 standard.
1050 International Laser Safety Conference. 2015;2015(1):75-7. doi: 10.2351/1.5056858.
1051 75. Geng Y, Dubra A, Yin L, Merigan WH, Sharma R, Libby RT, et al. Adaptive optics retinal
1052 imaging in the living mouse eye. Biomedical optics express. 2012;3(4):715-34. Epub 2012/05/11.
1053 doi: 10.1364/boe.3.000715. PubMed PMID: 22574260; PubMed Central PMCID:
1054 PMCPMC3345801.
1055 76. Atchison DA, Smith G. Chromatic dispersions of the ocular media of human eyes. J Opt
1056 Soc Am A. 2005;22(1):29-37. doi: 10.1364/JOSAA.22.000029.
1057 77. Nelder JA, Mead R. A Simplex Method for Function Minimization. The Computer Journal.
1058 1965;7(4):308-13. doi: 10.1093/comjnl/7.4.308.
1059 78. Baron WS. Maxwellian view stimulator for electrophysiological or psychophysical work.
1060 Applied optics. 1973;12(11):2560-2. Epub 1973/11/01. doi: 10.1364/AO.12.002560. PubMed
1061 PMID: 20125830.
1062 79. Schnapf JL, Kraft TW, Nunn BJ, Baylor DA. Spectral sensitivity of primate photoreceptors.
1063 Vis Neurosci. 1988;1(3):255-61. Epub 1988/01/01. PubMed PMID: 3154798.
1064 80. Snodderly DM, Auran JD, Delori FC. The macular pigment. II. Spatial distribution in
1065 primate retinas. Invest Ophthalmol Vis Sci. 1984;25(6):674-85. Epub 1984/06/01. PubMed PMID:
1066 6724837.
1067 81. Snodderly DM, Brown PK, Delori FC, Auran JD. The macular pigment. I. Absorbance
1068 spectra, localization, and discrimination from other yellow pigments in primate retinas. Invest
1069 Ophthalmol Vis Sci. 1984;25(6):660-73. Epub 1984/06/01. PubMed PMID: 6724836.
1070 82. Boettner EA. Spectral Transmission of the Eye. The University of Michigan, Final Report,
1071 Air Force Contract F41(609)-2966. 1967.
1072 83. Lamb TD. Photoreceptor spectral sensitivities: Common shape in the long-wavelength
1073 region. Vision Research. 1995;35(22):3083-91. doi: https://doi.org/10.1016/0042-
1074 6989(95)00114-F.

1075 84. Govardovskii VI, Fyhrquist N, Reuter TOM, Kuzmin DG, Donner K. In search of the visual
1076 pigment template. Visual Neuroscience. 2000;17(4):509-28. Epub 2000/07/01. doi:
1077 10.1017/S0952523800174036.
1078 85. Bowmaker JK. Cone Visual Pigments in Monkeys and Humans. Advances in
1079 Photoreception: Proceedings of a Symposium on Frontiers of Visual Science: National Academies
1080 Press; 1990.
1081 86. Dobkins KR, Thiele A, Albright TD. Comparison of red-green equiluminance points in
1082 humans and macaques: evidence for different L:M cone ratios between species. Journal of the
1083 Optical Society of America A, Optics, image science, and vision. 2000;17(3):545-56. Epub
1084 2000/03/09. PubMed PMID: 10708036.
1085 87. Estevez O, Spekreijse H. The "silent substitution" method in visual research. Vision Res.
1086 1982;22(6):681-91. Epub 1982/01/01. doi: 10.1016/0042-6989(82)90104-3. PubMed PMID:
1087 7112962.
1088 88. Brainard DH. The Psychophysics Toolbox. Spat Vis. 1997;10(4):433-6. Epub 1997/01/01.
1089 PubMed PMID: 9176952.
1090 89. Passaglia CL, Troy JB, Rüttiger L, Lee BB. Orientation sensitivity of ganglion cells in
1091 primate retina. Vision Research. 2002;42(6):683-94. doi: https://doi.org/10.1016/S0042-
1092 6989(01)00312-1.
1093 90. Yang Q, Zhang J, Nozato K, Saito K, Williams DR, Roorda A, et al. Closed-loop optical
1094 stabilization and digital image registration in adaptive optics scanning light ophthalmoscopy.
1095 Biomedical optics express. 2014;5(9):3174-91. Epub 2014/11/18. doi: 10.1364/boe.5.003174.
1096 PubMed PMID: 25401030; PubMed Central PMCID: PMCPMC4230869.
1097 91. Enroth-Cugell C, Robson JG. The contrast sensitivity of retinal ganglion cells of the cat. J
1098 Physiol. 1966;187(3):517-52. Epub 1966/12/01. doi: 10.1113/jphysiol.1966.sp008107. PubMed
1099 PMID: 16783910; PubMed Central PMCID: PMCPMC1395960.
1100 92. Cottaris NP, Jiang H, Ding X, Wandell BA, Brainard DH. A computational-observer model
1101 of spatial contrast sensitivity: Effects of wave-front-based optics, cone-mosaic structure, and
1102 inference engine. Journal of Vision. 2019;19(4):8-. doi: 10.1167/19.4.8.
1103 93. Cottaris NP, Wandell BA, Rieke F, Brainard DH. A computational observer model of
1104 spatial contrast sensitivity: Effects of photocurrent encoding, fixational eye movements, and
1105 inference engine. Journal of Vision. 2020;20(7):17-. doi: 10.1167/jov.20.7.17.
1106 94. Stockman A, Sharpe LT, Fach C. The spectral sensitivity of the human short-wavelength
1107 sensitive cones derived from thresholds and color matches. Vision Res. 1999;39(17):2901-27.
1108 Epub 1999/09/24. doi: 10.1016/s0042-6989(98)00225-9. PubMed PMID: 10492818.
1109 95. Stockman A, Sharpe LT. The spectral sensitivities of the middle- and long-wavelength-
1110 sensitive cones derived from measurements in observers of known genotype. Vision Research.
1111 2000;40(13):1711-37. doi: https://doi.org/10.1016/S0042-6989(00)00021-3.
1112 96. Pokorny J, Smith VC, Lutze M. Aging of the human lens. Applied optics. 1987;26(8):1437-
1113 40. doi: 10.1364/AO.26.001437.
1114 97. Dalkara D, Kolstad KD, Caporale N, Visel M, Klimczak RR, Schaffer DV, et al. Inner limiting
1115 membrane barriers to AAV-mediated retinal transduction from the vitreous. Molecular therapy :
1116 the journal of the American Society of Gene Therapy. 2009;17(12):2096-102. Epub 2009/08/13.
1117 doi: 10.1038/mt.2009.181. PubMed PMID: 19672248; PubMed Central PMCID:
1118 PMCPMC2814392.
1119 98. McGregor JE, Godat T, Dhakal K, Parkins K, Strazzeri J, Bateman B, et al. Optogenetic
1120 restoration of retinal ganglion cell activity in the living primate. Nature Communications. 2020.

1121 99. Helga Kolb EF, Ralph N. Webvision : the organization of the retina and visual system:
1122 [Bethesda, Md.] : National Library of Medicine : [National Center for Biotechnology
1123 Information], 2007.; 2007.
1124 100. Croner LJ, Purpura K, Kaplan E. Response variability in retinal ganglion cells of primates.
1125 Proceedings of the National Academy of Sciences. 1993;90(17):8128-30. doi:
1126 10.1073/pnas.90.17.8128.
1127 101. Yan W, Peng Y-R, van Zyl T, Regev A, Shekhar K, Juric D, et al. Cell Atlas of The Human
1128 Fovea and Peripheral Retina. Scientific reports. 2020;10(1):9802. doi: 10.1038/s41598-020-
1129 66092-9.
1130 102. Provis JM, Hendrickson AE. The Foveal Avascular Region of Developing Human Retina.
1131 Archives of Ophthalmology. 2008;126(4):507-11. doi: 10.1001/archopht.126.4.507.
1132 103. De Valois RL, Morgan H, Snodderly DM. Psychophysical studies of monkey Vision-III.
1133 Spatial luminance contrast sensitivity tests of macaque and human observers. Vision Research.
1134 1974;14(1):75-81. doi: https://doi.org/10.1016/0042-6989(74)90118-7.
1135 104. van der Schaaf A, van Hateren JH. Modelling the Power Spectra of Natural Images:
1136 Statistics and Information. Vision Research. 1996;36(17):2759-70. doi:
1137 https://doi.org/10.1016/0042-6989(96)00002-8.
1138 105. Lee BB, Sun H. The chromatic input to cells of the magnocellular pathway of primates.
1139 Journal of vision. 2009;9(2):1-18. doi: 10.1167/9.2.15. PubMed PMID: 19271925.
1140 106. Bumsted K, Hendrickson A. Distribution and development of short-wavelength cones
1141 differ between Macaca monkey and human fovea. J Comp Neurol. 1999;403(4):502-16. Epub
1142 1999/01/15. PubMed PMID: 9888315.

1143

Figures and Tables

Figure 1.

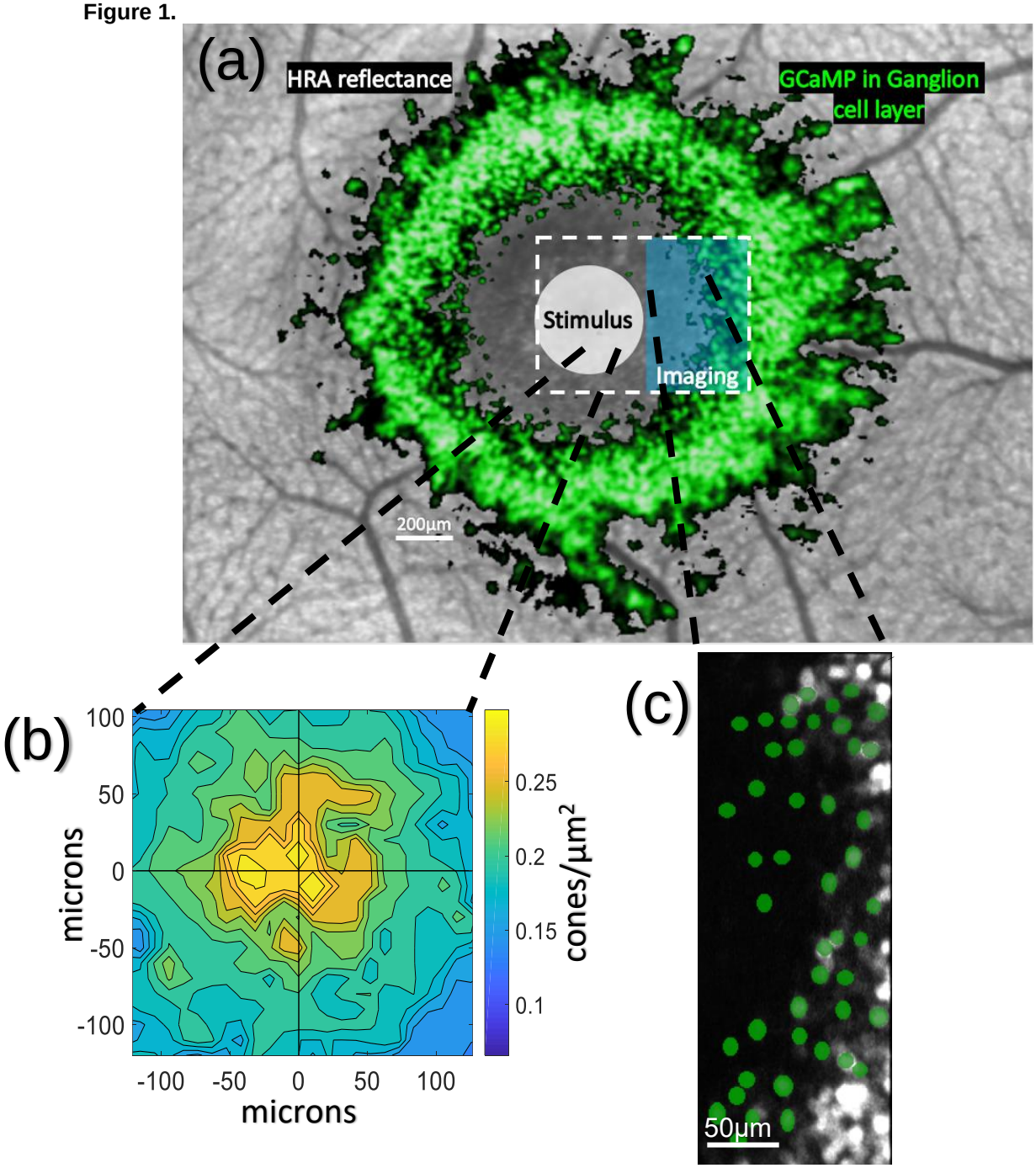

Fig 1. Stimulus presentation and recording paradigm. In (a) the general stimulation paradigm is shown. Background is an image of the M3 using the blue reflectance imaging modality of a Heidelberg Spectralis instrument. In false color green are GCaMP-expressing cells from M3 imaged using the blue autofluorescence modality of the same Spectralis instrument. When using the AOSLO instrument, videos are captured within one rectangular field of view (white dashed line) while stimuli (white circle) such as cone-isolating flicker or drifting gratings are presented to the centermost foveal cone photoreceptors. An imaging laser in the AOSLO (blue rectangle) excites GCaMP-mediated fluorescent responses of ganglion cells surrounding the foveal slope. (b) shows the recorded cone densities at the fovea of M3 and (c) shows the ganglion cells segmented (green) at the innermost edge of the foveal slope in M3.

Figure 2.

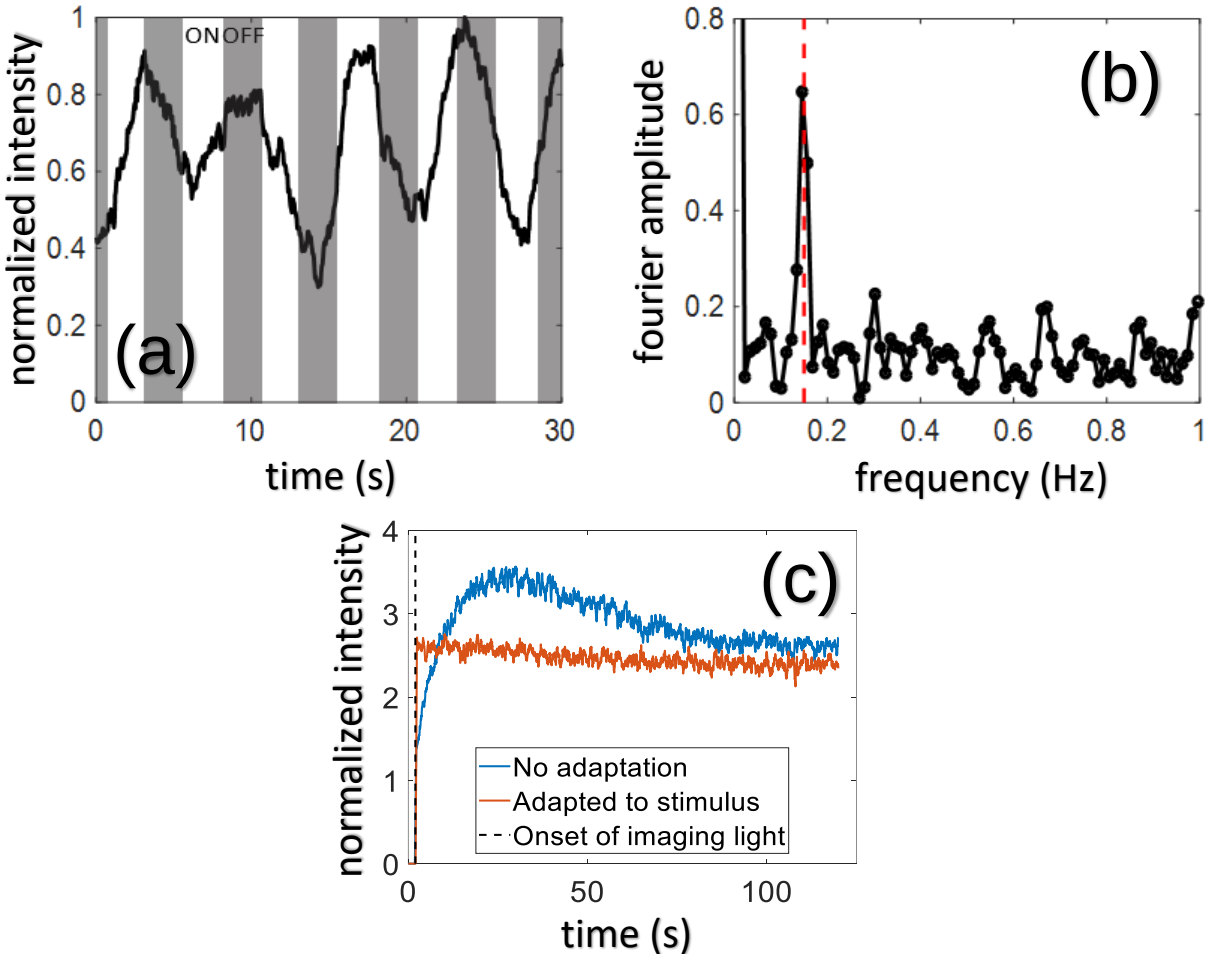

Fig 2. Data collection from ganglion cells *in vivo*. (a) shows the smoothed timecourse of a single RGC fluorescence response to a 0.15Hz luminance flicker stimulus. (b) shows the Fourier transform of the response timecourse, recovering the response peak at the stimulus frequency of 0.15Hz (red dashed line). (c) shows the effect of the imaging light on cone-mediated response to stimuli in 62 foveal RGCs. The 488nm imaging laser which excites GCaMP fluorescence can scatter to foveal cones and confound cone stimulation. If the imaging light is turned on without adaptation, there is a quick rise and slow falloff in fluorescence due to cone responses feeding RGCs. However, if the 561nm stimulus laser (used for drifting gratings) is presented at a mean luminance of 2-2.5 μW during a short 30s adaptation period prior to imaging onset, then there is no corresponding effect of the imaging light confounding the fluorescence signal. In all recordings, an adaptation light preceded each recording to prevent this transient effect from scattered light from the imaging laser.

Figure 3.

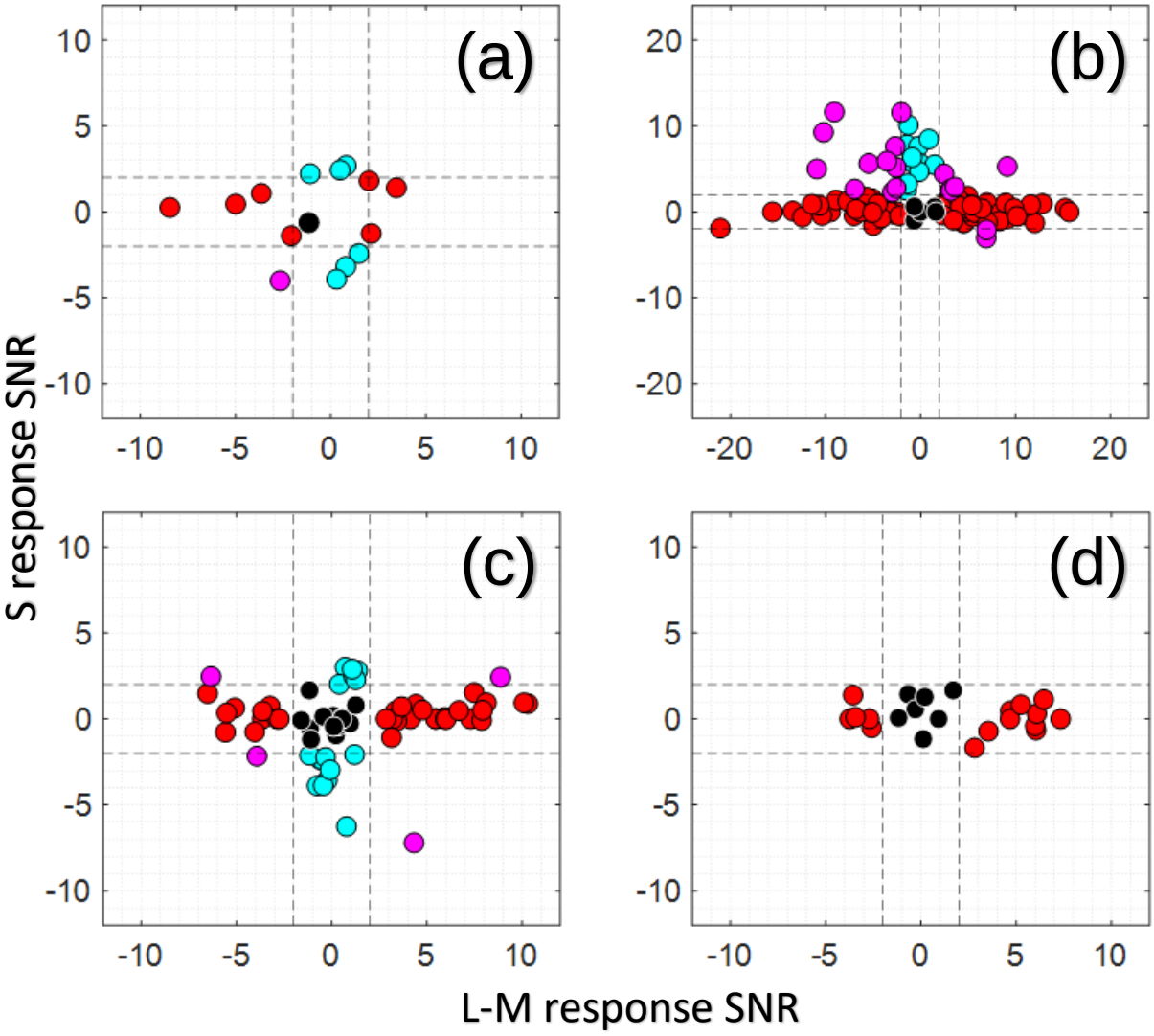

Fig 3. Chromatic response properties of RGCs from three different animals. Black dots show luminance only responding cells, red dots show L/M chromatic opponent cells, blue dots show S responding cells, while magenta dots show cells that responded to both L/M and S stimuli. Cell response is captured by our signal-to-noise metric which is similar to the sensitivity index d' and was calculated in the following way: the Fourier amplitudes of each cell at the stimulus frequency (0.15 Hz or 0.2 Hz) were normalized by subtracting out the mean noise at higher frequencies (0.32Hz to 1.08Hz) and then dividing by the standard deviation of the noise. Response phases were also calculated but are not directly shown; however, positive SNRs correspond to responses that were in phase with that stimulus presentation (ON response), while negative SNRs correspond to responses that were approximately 180deg out of phase with stimulus presentation (OFF response). The luminance axis would be out of the page and is not included for readability and because not all cells responded to the luminance stimulus, so luminance only cells in black include both ON and OFF cells. In (a), responses from 15 cells in M1 are shown after presentation of spatially uniform luminance, L-M isoluminant and S-isolating stimuli at 0.2 Hz. In (b), responses from 126 cells in M2 are shown after presentation of spatially uniform luminance, L-M isoluminant and S-isolating stimuli at 0.2 Hz. In (c), responses from 83 cells in M3 are shown after presentation of spatially uniform luminance, L-isolating, M-isolating, and S-isolating stimuli at 0.15 Hz. In (d), responses from 22 cells serving the very central fovea of M3 are shown after presentation of spatially uniform luminance, L-isolating, M-isolating, and S-isolating stimuli at 0.15 Hz. These cells are closer to the foveal center than any of the cells shown in (c). In (c-d), all stimuli were single-cone isolating, so the L-M x-axis is calculated from the single cone L-isolating and M-isolating responses and their relative phase.

Figure 4.

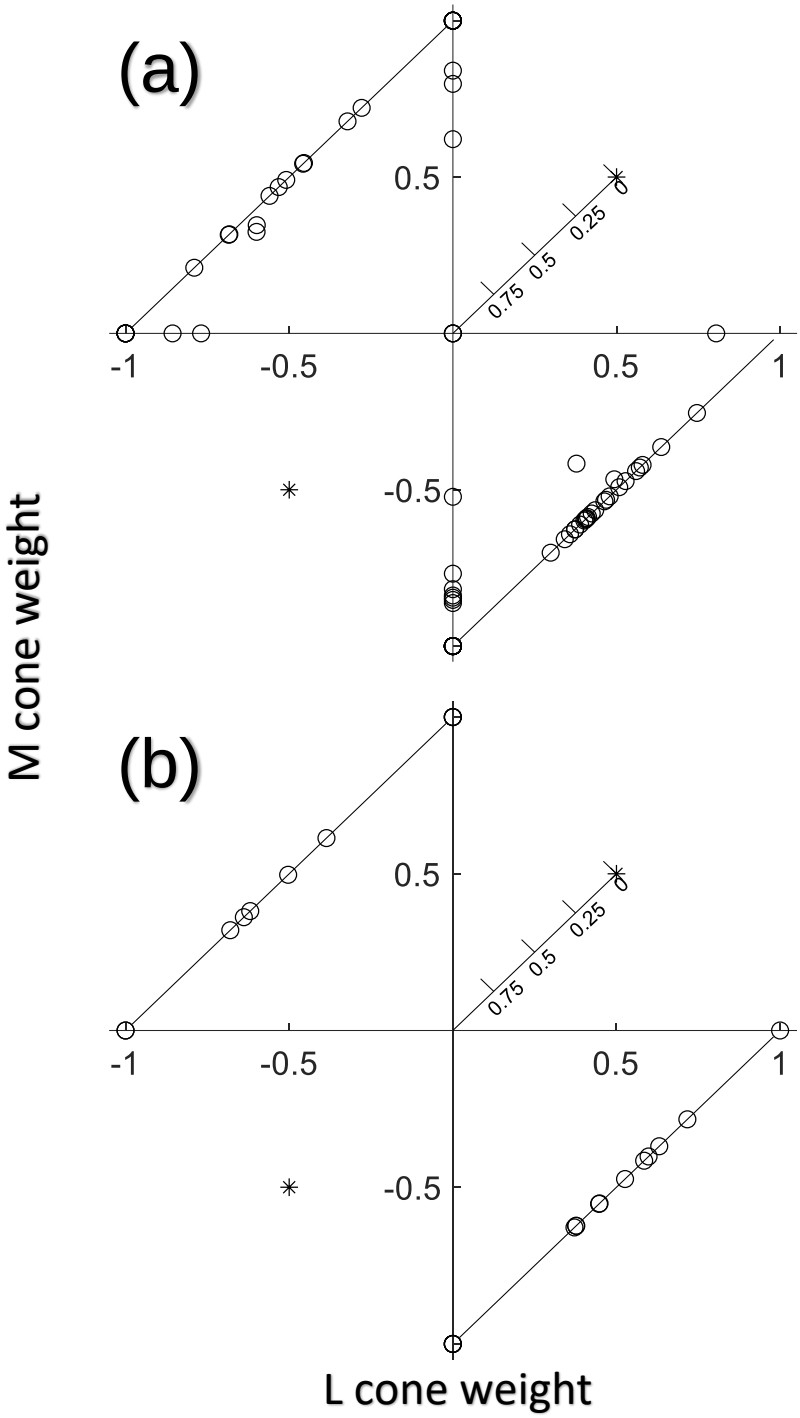

Fig 4. Cone weights of RGCs from M3. The horizontal axis shows L cone weight, the vertical axis the M cone weight, and the distance from the origin shows the S cone weight where further away from the origin corresponds to less S-cone weighting. In (a), 100 RGCs were recorded across the entire width of the GCaMP-expressing ring. There were 3 cells that only showed S cone responses, represented by overlapping circles at the origin. There were also 4 L+M and 11 -L-M luminance only cells that are represented by asterisks in the upper right and lower left. Because these cells only responded to the luminance stimulus but not the L-isolating or M-isolating stimulus, the response sign is known but not the exact L/M cone weighting. In (b), 34 cells at the innermost edge of the foveal slope, served by the centralmost foveal cones, were recorded from. No consistent S only responses were observed, and there were 5 L+M and 2 -L-M luminance only cells.

Figure 5.

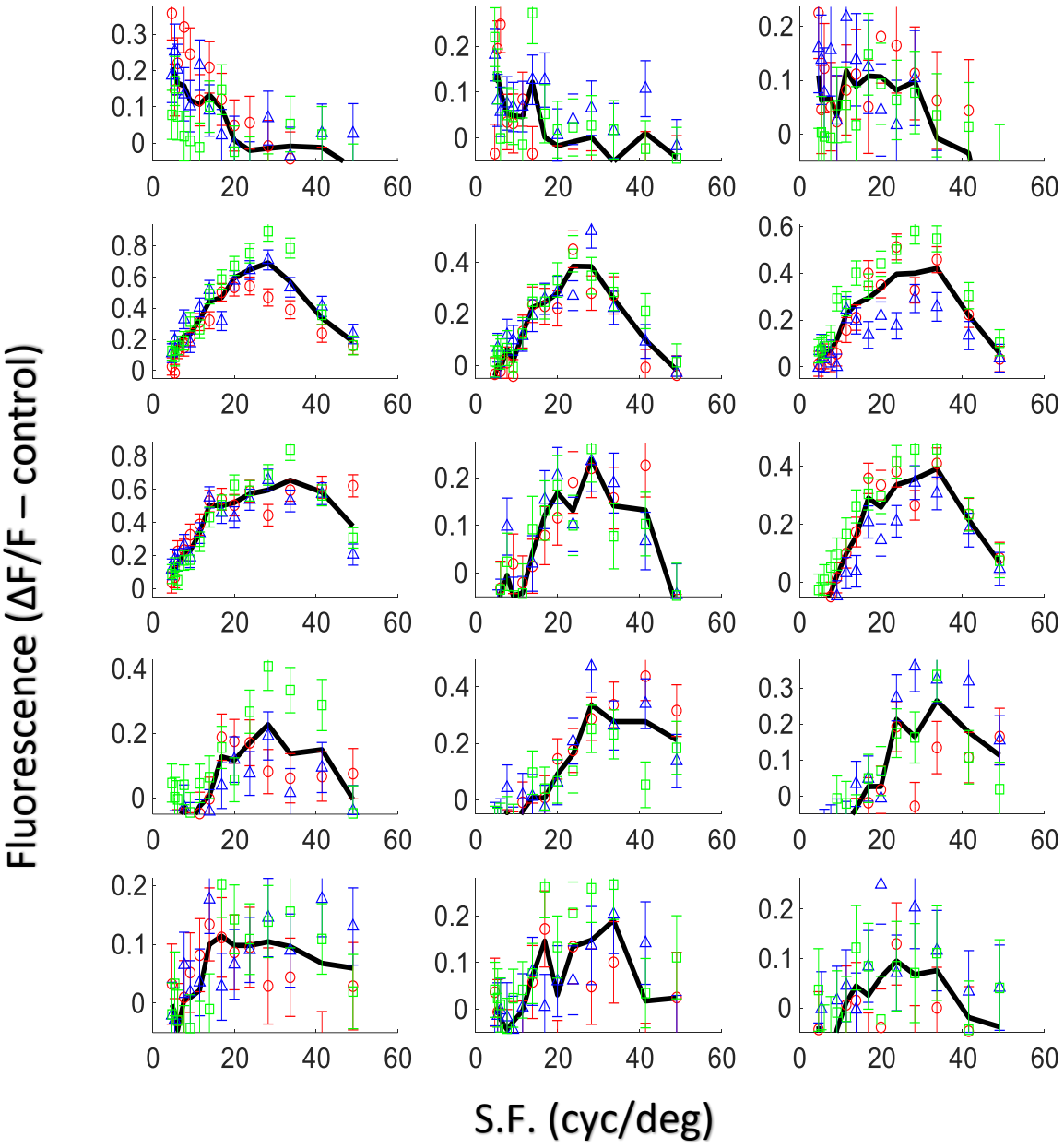

Fig 5. Spatial frequency responses of putative midget cells. Fifteen cells in M3 serving the central foveal cones were identified as L/M chromatic opponent. Drifting gratings were presented at 561 nm to the photoreceptors and ganglion cell fluorescence was elicited using a 488 nm imaging laser. The green points (squares), blue points (triangles), and red points (circles) are measurements from three different experiments each exactly week apart. The solid black line in each panel is the average response for that particular cell across all three experiments. The vertical axis is a response metric where the mean baseline fluorescence is subtracted from the fluorescence under stimulation and divided by the fluorescence under stimulation at the peak spatial frequency. Controls were also subtracted from the response metric for each experiment. The error bars show the standard error at each data point, which represents the error in obtaining the signal and background needed to calculate the metric.

Figure 6.

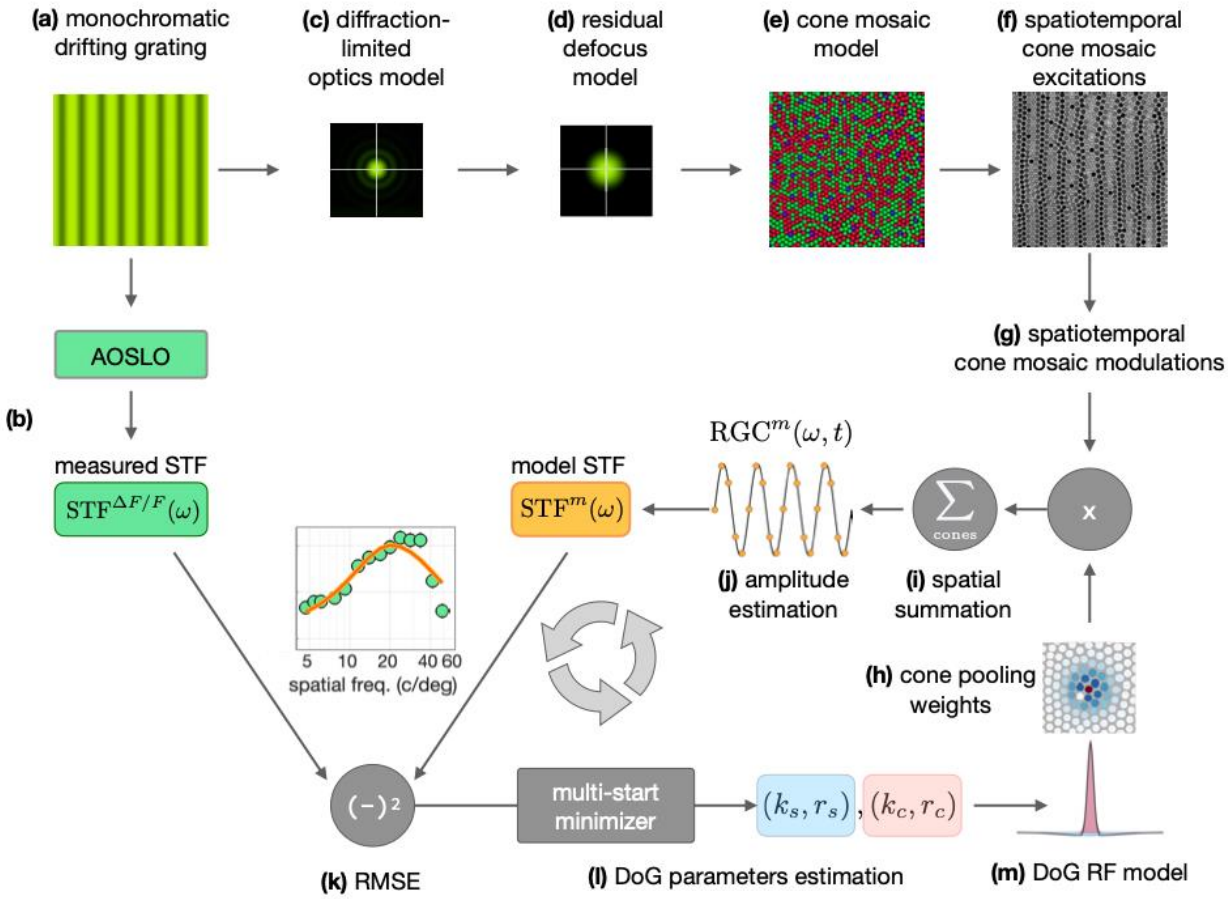

Fig 6. Schematic overview of the ISETBio modeling approach. To interpret the AOSLO-based STF measurements in terms of the spatial pooling of cone signals to the measured RGCs we model the spatial, spectral and temporal aspects of the stimulus, the optics, the cone mosaic and the cone pooling within the center and surrounds mechanisms of an RGC using the ISETBio toolbox. **(a)** A frame of the drifting monochromatic grating stimulus which is projected via the AOSLO system to stimulate and measure the Ca^{2+}-fluorescence – based spatial transfer function (STF) of RGCs, $STF^{\Delta F/F}(\omega)$ **(b).** The drifting grating is modeled as a temporal sequence of spatial spectral radiance scenes. These scenes are passed via a model of the AOSLO system which includes a diffraction-limited optical system with a 6.7 mm pupil **(c)** combined with a residual defocus system **(d).** The resulting sequence of retinal irradiance maps are spectrally integrated and spatially averaged within the apertures of cones in a model of the animal's cone mosaic **(e)**, resulting in a spatiotemporal sequence of cone excitations **(f).** Cone excitations are transformed to cone modulations by first subtracting and subsequently dividing the mean cone excitation level **(g).** Modulation signals from different cones are scaled by the spatial weights with which the RF center and the RF surround mechanism pool cone signals **(h).** The weighted cone signals are subsequently summed **(i)** to compute the temporal response of the model RGC. A sinusoid is fitted to the RGC temporal response **(j)** and the amplitude of the sinusoid is taken as the STF of the model RGC at the stimulus spatial frequency, $STF^{m}(\omega)$. The RMSE between $STF^{m}(\omega)$ and $STF^{\Delta F/F}(\omega)$ **(k)** is minimized using a multi-start solver which optimizes the center and surround peak sensitivity and radius parameters **(l)** of a DoG RF model **(m).** Finally, the DoG RF model is sampled by the cone mosaic, thereby yielding the optimal cone pooling weights for the model RGC.

Figure 7.

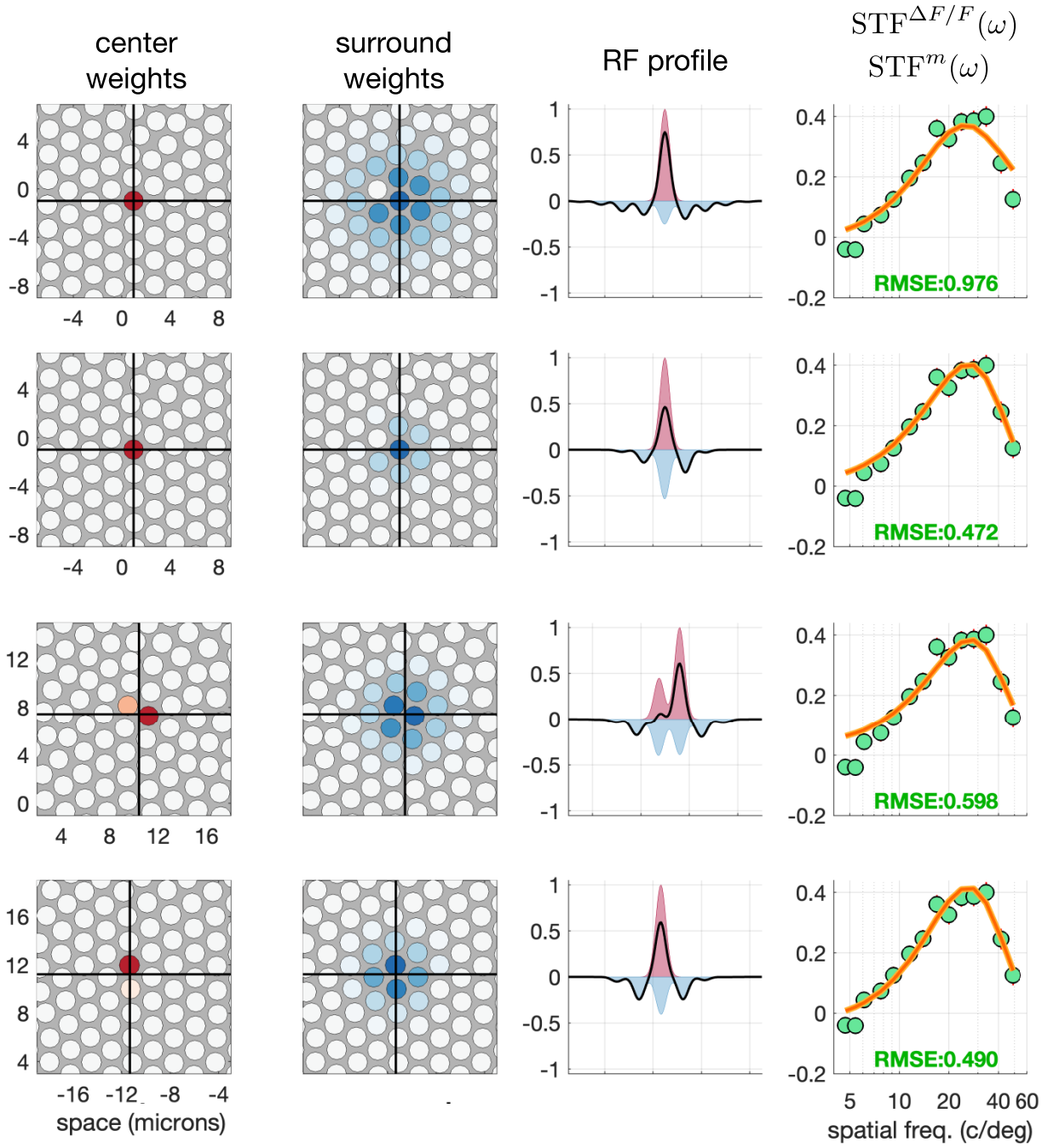

Figure 7. ISETBio-model receptive field estimates for one RGC derived by the four examined scenarios. The single-cone RF center with zero and 0.067D residual AOSLO defocus scenarios are depicted in the first and second row, respectively. The multi-cone RF center with zero and 0.067D residual AOSLO defocus scenarios are depicted in the third and fourth row, respectively. The first and second columns depict the spatial distribution of cone pooling weights for the RF center and surround mechanism, respectively. Red and blue hues indicate positive and negative polarity, respectively, and saturation indicates pooling strength. The red and blue histograms in the third column depict the RF center and surround profiles, computed by integrating along the y-axis the weighted apertures of cones feeding into the center and surround mechanism, respectively, whereas the black lines depict the composite RF profile (center-surround. The green disks and the orange line in fourth column depict the fluorescence-based STF, and the STF of the fitted model, respectively, with the RMSE of the fit displayed in green.

Figure 8.

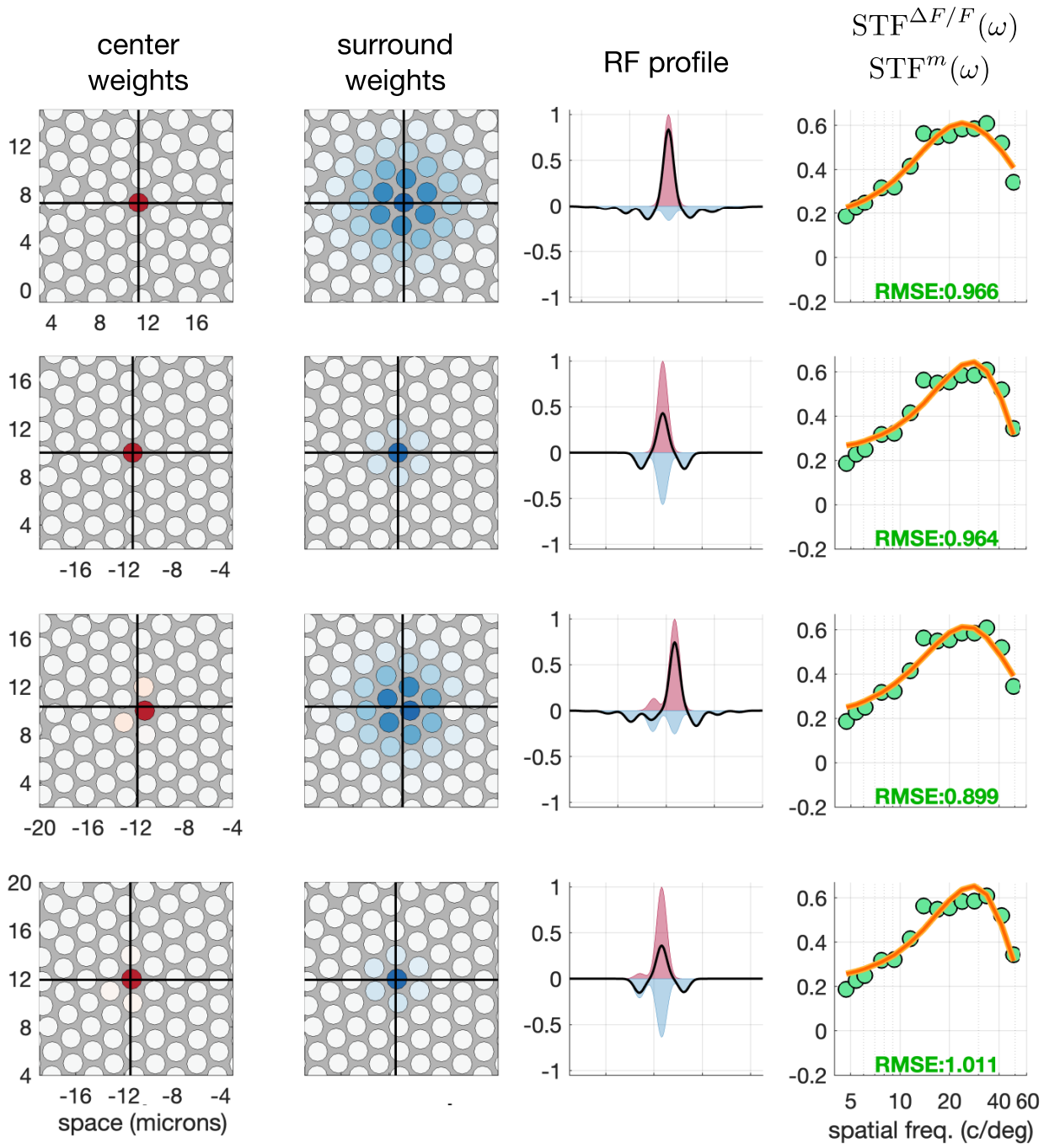

Figure 8. ISETBio-model receptive field estimates for a second RGC derived by the four examined scenarios. Unlike the RGC depicted in Figure 7, in this RGC all four examined scenarios perform similarly in terms of the RMSE between the predicted STF and the measured STF. Here, the 2 scenarios with zero residual defocus (rows 1 and 3), predict a large surround, where the 2 scenarios with 0.067D residual defocus (rows 2 and 4) predict a much more focal surround. Also, the multi-cone RF center scenarios (rows 3 and 4) assign very small weights to the non-dominant center cones, essentially collapsing to their single cone RF center counterparts.

.

Figure 9.

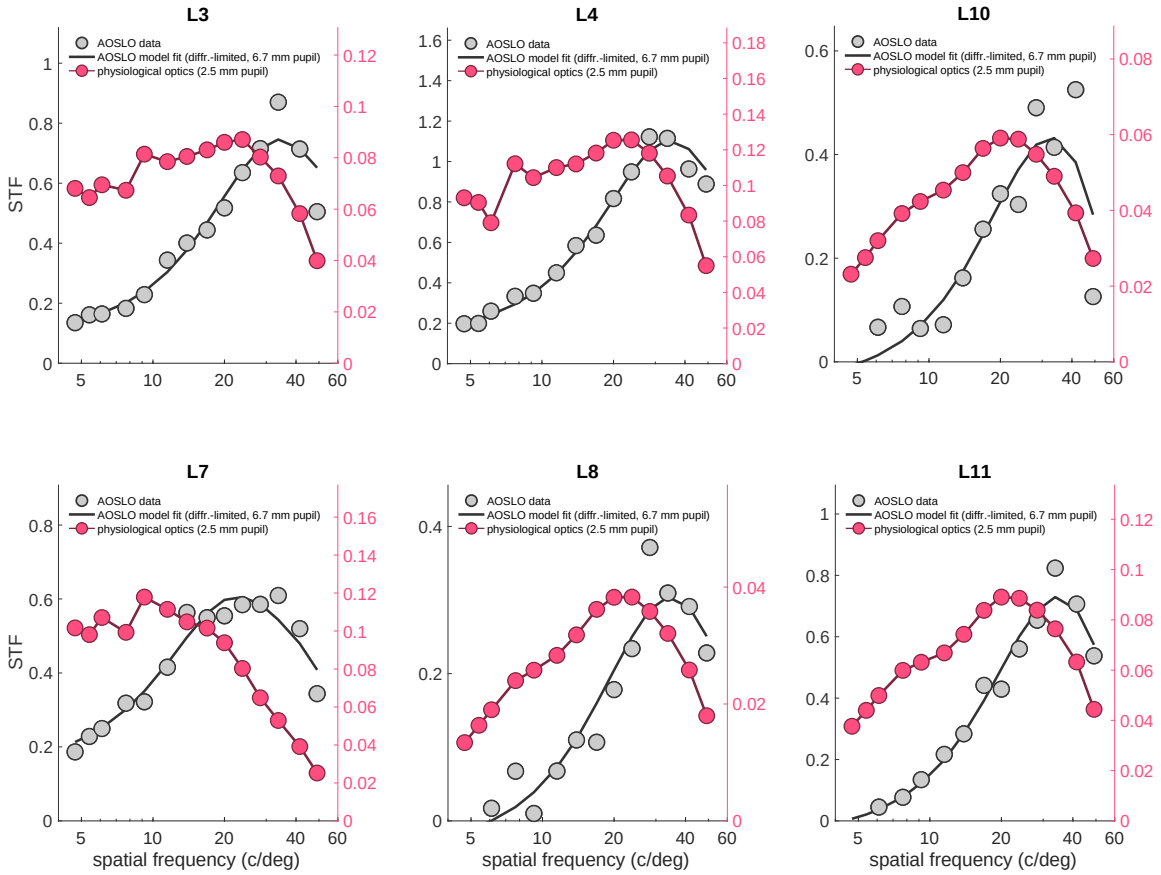

Figure 9. STFs measured under diffraction-limited optics vs. STF measured under normal physiological optics. Gray disks depict STF data measured using diffraction-limited optics and a 6.7 mm pupil and black lines depict the STF of the best-fit ISETBio model. The receptive field model derived by the best-fit model is subsequently used to predict the STF of the same cell under the animal's physiological optics as characterized by wavefront-aberration measurements, with a 2.5 mm pupil. These STFs are depicted by the red disks. Note that normal optics shift the STF peak to lower spatial frequencies and significantly reduce the low spatial frequency attenuation seen under diffraction-limited optics.

Figure 10.

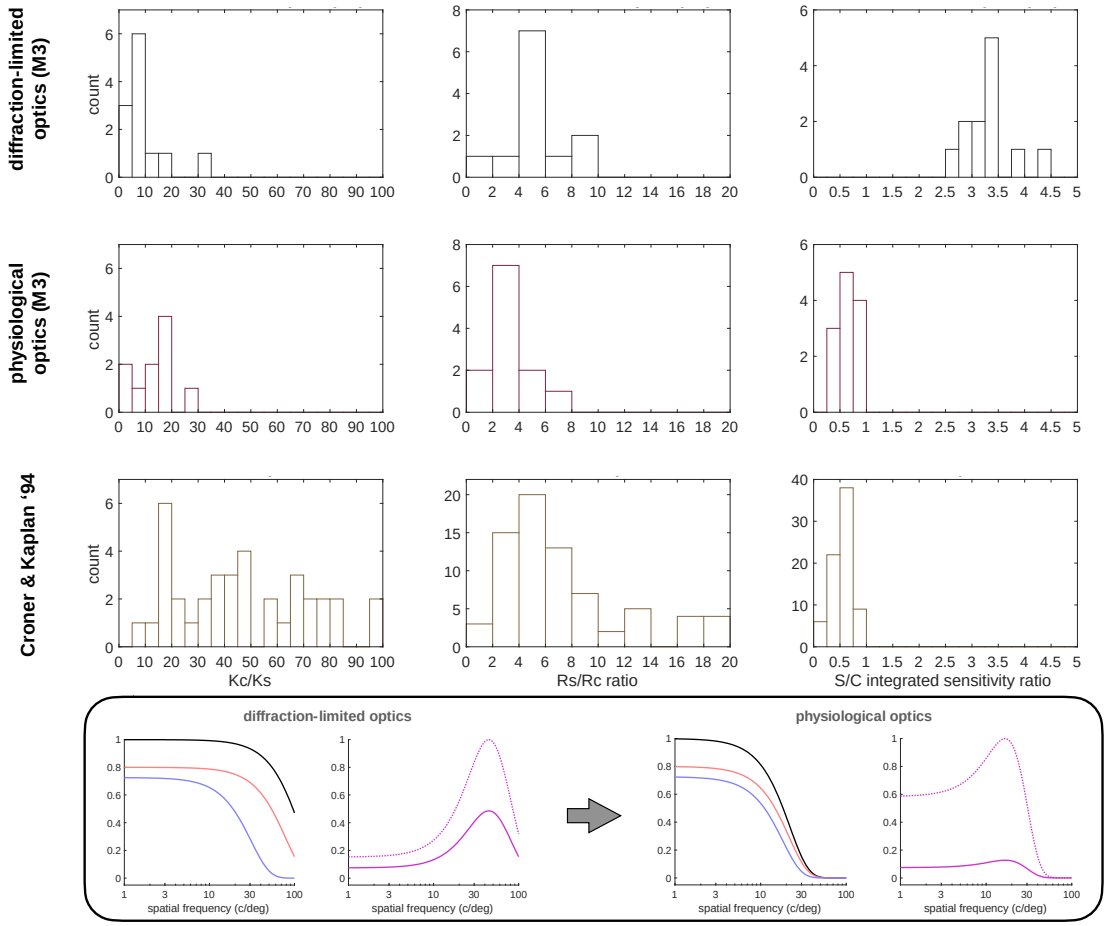

Figure 10. How the spatial structure of retinal receptive fields gets transformed by physiological optics. The diffraction-limited STF and the STF derived under physiological optics (Figure 9) are fitted with a DoG RF model. Depicted here are three key characteristics of this model: the ratio of center-to-surround peak sensitivities (left column), the ratio of surround-to-center characteristic radii (middle column) and the ratios of surround-to-center integrated sensitivities (right column). The top row depicts results obtained under diffraction-limited optics in the population of the 15 foveal cells recorded in M3. The middle row depicts the same data modified by simulating physiological optical conditions using the animal's own wavefront aberration optics, again in the same population of the 15 foveal cells. The bottom row depicts results of Croner&Kaplan '94, in a population of animals in which RGCs were recorded at a wide range of eccentricities under physiological optics. Compared to the results obtained under physiological optics in M3, we see that under diffraction-limited optics the Kc/Ks ratios are smaller and the Rs/Rc ratios are somewhat larger. The two factors combine in such a way that under diffraction-limited optics the median integrated sensitivity of the surround is 3.3 times stronger than the integrated sensitivity of the center. In sharp contrast, under physiological optics, the median integrated sensitivity of the RF surround is on average 0.7 the sensitivity of the RF center, both in our M3 population and in the population of Croner&Kaplan. This change in center/surround balance is purely a manifestation of the differential effect of optics (black like at the inset) on the center MTF (red line) as compared to the surround MTF (blue line), which transforms the MTF of RGCs (purple lines) from strongly bandpass, under diffraction-limited optics, to weakly bandpass under physiological optics.